Phase equilibria modelling constraints on the *P*–*T* conditions of eclogitised granulite in the Bergen Arcs, Norway

Thesis submitted in accordance with the requirements of the University of Adelaide for an Honours Degree in Geology

Kamini Bhowany

November 2015

THE UNIVERSITY of ADELAIDE

PHASE EQUILIBRIA MODELLING CONSTRAINTS ON THE *P–T* CONDITIONS OF ECLOGISTISED GRANULITE IN THE BERGEN ARCS, NORWAY

RUNNING TITLE: *P–T* CONSTRAINTS OF ECLOGITISED GRANULITES

ABSTRACT

Exhumed deep crust is rare and exposures that preserve both protoliths and altered domains are limited around the world. Mesoproterozoic anorthositic granulites exposed on the island of Holsnøy, western Norway, preserve different stages of progressive deformation together with the corresponding metamorphism that record the conversion to Siluro-Ordovician eclogites during fluid infiltration. Five different stages of deformation can be identified: 1) brittle deformation resulting in the formation of fractures and generation of pseudotachylites in the granulite; 2) development of mesoscale shear zones associated with increased fluid–rock interaction; 3) large-scale replacement of granulite by hydrous eclogite with blocks of granulite sitting in an eclogitic 'matrix'; 4) complete conversion of granulite to eclogite within large-scale shear zones; and 5) break up of completely eclogitised granulite by continued fluid influx, resulting in the formation of potassium-rich mineral assemblages. *P–T* constraints derived from phase equilibria forward modelling document a burial and partial exhumation path with peak conditions around 21–22 kbar and 640–660 °C. Fluid infiltration began on the prograde path and continued throughout the recorded *P–T* evolution. However, in places limited fluid availability on the prograde path resulted in an excellent preservation of prograde mineral assemblage, allowing the burial path to be well constrained.

KEYWORDS

Eclogite; fluid assisted metamorphism; *P–T* pseudosections; Caledonian Orogeny; Bergen Arcs; *P–T* path

TABLE OF CONTENTS

List of Figures and Table 2
1. Introduction 3
2. Geological Setting 5
2.1. Study area 5
2.2. Structural features and stages of deformation. 6
3. Methods 12
3.1. Detailed mapping and sample collection 12
3.2. Bulk-rock and mineral chemistry 13
3.3. Phase equilibria forward modelling 13
3.3.1. Bulk-rock composition determination 13
3.3.2. Pressure–temperature pseudosections 14
3.3.3. Contours of phase chemistry 15
4. Results 16
4.1. Petrography 16
4.2. Whole-rock geochemistry and Mineral chemistry 20
4.3. Pressure-Temperature conditions 27
4.3.1. HOL2A_2015 (recrystallised pseudotachylite) 27
4.3.2. HOL7C_2014 (complete eclogitisation) 28
4.3.3. HOL13A_2015 (mica-rich eclogite) 30
5. Discussion 32
5.1. Pressure–Temperature evolution 32
5.2. *P–T* constraints and fluid infiltration 35
5.3. Tectonic significance of fluid infiltration. 36
6. Conclusions 38
7. Acknowledgments 38
8. References 39
Appendix A: Detailed Pseudosections 44
Appendix B: Additional contours for Hol7C_2014 and HOL13A_2015 47
Appendix C: Additional X-ray maps 48
Appendix E: Addition microprobe analysis data 48

LIST OF FIGURES AND TABLES

List of Figures and Tables....2
Figure 1. Location map of Holsnøy in the Bergen Arcs and distribution of domains on the island....5
Figure 2. Field outcrops of granulite....6
Figure 3. Features of Stage 1 deformation....8
Figure 4. Features of Stage 2 deformation....9
Figure 5. Features of Stage 3 deformation....10
Figure 6. Features and model of Stage 4 deformation....11
Figure 7. Features and domains of Stage 5 deformation....10
Figure 8. Photomicrographs of key petrological relationships in samples....17
Table 1. Bulk-rock composition data in wt %....20
Table 2. Bulk-rock composition data in mol % (THERMOCAL input)....20
Figure 9. Electron microprobe X-ray maps of HOL7C_2014....22
Table 3. Representative electron microprobe data of garnet in HOL7C_2014....23
Figure 10. Compositional profile across garnet in HOL7C_2014....24
Table 4. Representative electron microprobe data of phengite in HOL7C_2014....25
Table 5. Representative electron microprobe data of omphacite in HOL7C_2014....26
Figure 11. Calculated *P–T* pseudosection for HOL2A_2015....27
Figure 12. Calculated *P–T* pseudosection for HOL7C*_2014....28
Figure 13. Calculated *P–T* pseudosection for modified compostion of HOL7C_2014....29
Figure 14. Calculated *P–T* pseudosection for HOL13A_2015....31
Figure 15. Summary of P-T evolution of the domains on Holsnøy....33
Figure 16. Model of progressive deformation on Holsnøy....37

1. INTRODUCTION

It is widely accepted that the conversion of granulite facies rocks to eclogites is controlled largely by changes in pressure and temperature (Lardeaux & Spalla 1991, Pearson *et al.* 1991, De Paoli *et al.* 2009). However, studies have also shown that the conversion of granulites to eclogites can be enhanced by the presence of fluids and deformation (Austrheim & Griffin 1985, Erambert & Austrheim 1993, Jolivet *et al.* 2005, Terry & Heidelbach 2006, Martin *et al.* 2011). The conversion of granulites with a nominally anhydrous mineralogy to hydrous eclogites is particularly intriguing in terms of the source of the fluid (Jamtveit *et al.* 1990, Andersen *et al.* 1993, Mattey *et al.* 1994, Van Wyck *et al.* 1996, Schulte & Sindern 2002, Russell *et al.* 2012). The replacement of anhydrous mineral assemblages by hydrous ones is important as the overprinting mineral assemblage may result in changes to the geodynamic response and behaviour of the system (Erambert & Austrheim 1993, Rockow *et al.* 1997, Engvik *et al.* 2000, Pollok *et al.* 2008, Connolly 2009). Moreover, fluid infiltration could also influence the geophysical signatures of the lower crust (Boundy *et al.* 1992, Austrheim *et al.* 1997, Bingen *et al.* 2001, Austrheim 2013).

On the island of Holsnøy in the Bergen Arcs, western Norway, white mica- and epidote-group-bearing (*i.e.* hydrous) eclogites occur extensively amongst granulitic protolith (Fig. 1). The anorthositic granulites are late Mesoproterozoic in age (c. 950Ma) whereas the eclogites are Ordovician-aged (c. 450Ma) (Van Wyck *et al.* 1996, Bingen *et al.* 2001, Bingen *et al.* 2004, Austrheim 2013). The production of the eclogites is interpreted to have occurred during fluid infiltration—a form of deep crustal metasomatism—along fractures and shear zones during the Caledonian Orogeny (Austrheim & Griffin 1985, Andersen *et al.* 1990, Boundy *et al.* 1992, Austrheim 2013). Mineralogically and geochemically, the evidence for fluid infiltration is confirmed by the presence of potassium-rich mica, epidote-group minerals and the presence of quartz veins within the hosting granulite (Austrheim & Griffin 1985,

Andersen *et al.* 1990, Andersen *et al.* 1991c, Boundy *et al.* 1992, Raimbourg *et al.* 2005, Austrheim 2013).

Numerous studies have investigated the development of the fluid–rock system on the exposures on Holsnøy (e.g. Austrheim & Griffin 1985, Andersen *et al.* 1991c, Bingen *et al.* 2001, Raimbourg *et al.* 2005, Russell *et al.* 2012, Austrheim 2013). However, there are few robust constraints on the pressure–temperature (*P–T*) conditions at which fluid–rock interaction occurred. Existing constraints of 15–21 kbar and 650–800 °C were derived from conventional thermobarometry (Fe–Mg exchange between garnet and omphacite and garnet and amphibole) (Austrheim & Griffin 1985, Jamtveit *et al.* 1990, Boundy *et al.* 1996, Boundy *et al.* 1997). However, conventional thermobarometry—especially that based on Fe–Mg exchange—is readily affected by retrograde resetting of mineral compositions (Frost & Chacko 1989, Fitzsimons & Harley 1994, Pattison *et al.* 2003, Hora *et al.* 2014), rendering the derived *P–T* estimates unreliable. The paucity of robust *P–T* information means that constraints on the conditions accompanying fluid–rock interaction leading to eclogite formation are few. Better constrained *P–T* information will provide a framework in which to understand the origins of the metasomatising fluids.

This study uses field structural relationships to identify different stages of deformation. Samples from these different stages are then used in mineral equilibria forward modelling to constrain the framework for the evolving *P–T* conditions under which the eclogitisation process occurred. The findings of this study have implications for the relative timing of fluid infiltration during subduction of the anhydrous granulitic crust during the Caledonian Orogeny, in the Bergen Arcs.

2. GEOLOGICAL SETTING

2.1. Study area

Holsnøy Island is located in south-western Norway, approximately 45 km north-west of Bergen (Fig. 1b). The outcropping rocks form part of the Lindås Nappe, which is one of the major domains of the Bergen Arcs (Austrheim 2013, Centrella *et al.* 2015). It is, arguably, one of the best locations in the world to study deep crust metasomatism, as both the protholith (granulite) and metamorphosed rock (eclogite) are superbly preserved (Raimbourg *et al.* 2005, Austrheim 2013, Centrella *et al.* 2015). This study focuses on north-eastern Holsnøy (Fig.1c), where the main eclogitised granulite can be found along with different deformational features.

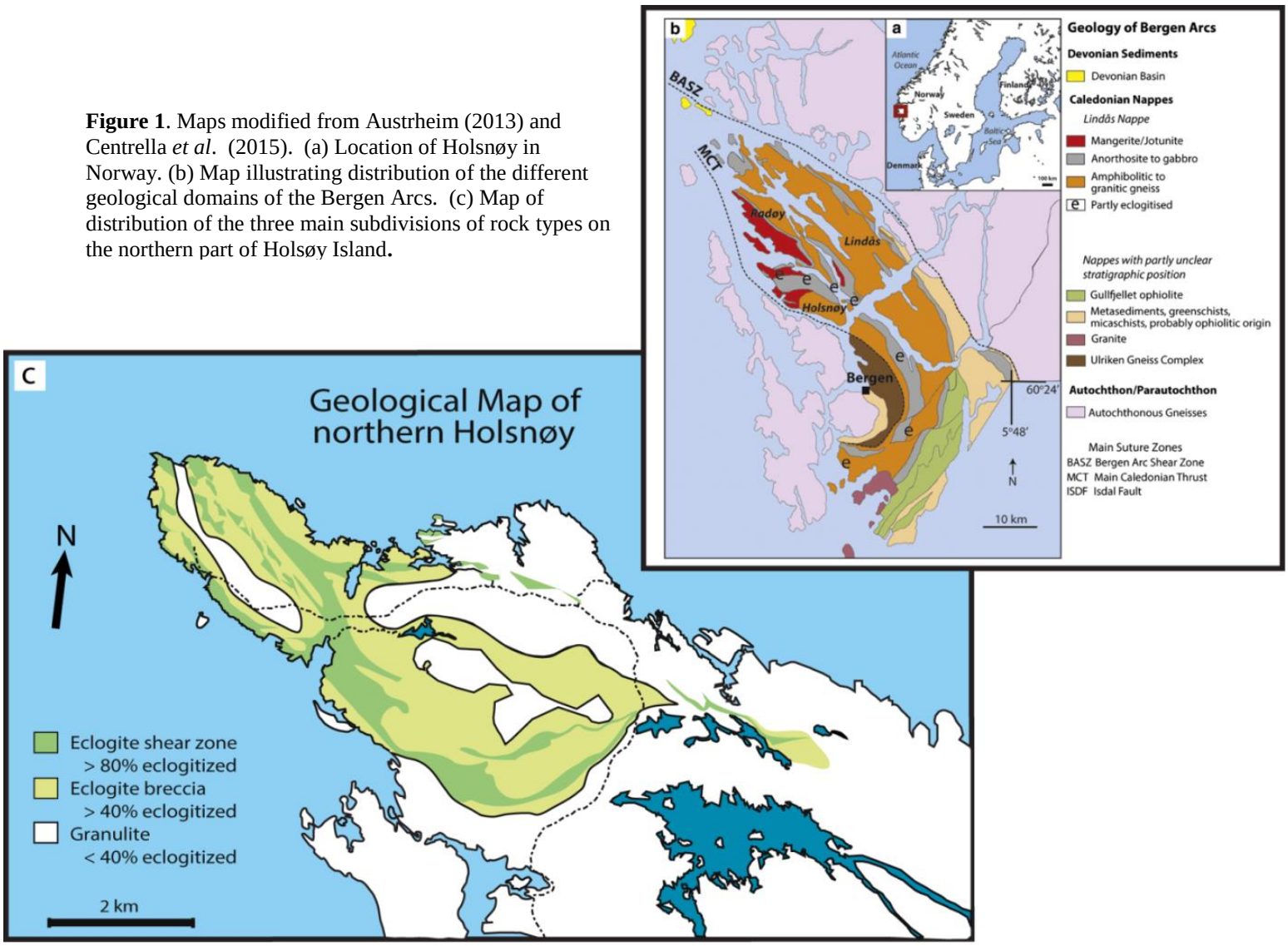

Figure 1. Maps modified from Austrheim (2013) and Centrella *et al*. (2015). (a) Location of Holsnøy in Norway. (b) Map illustrating distribution of the different geological domains of the Bergen Arcs. (c) Map of distribution of the three main subdivisions of rock types on the northern part of Holsøy Island**.**

2.2. Structural features and stages of deformation.

The granulite-facies, anorthositic protolith was metamorphosed at approximately 950 Ma (Krogh 1977, Austrheim & Griffin 1985, Pollok *et al.* 2008) during the Grenvillian-aged Sveconorwegian Orogeny (Austrheim & Griffin 1985, Austrheim 1987). The granulite is dominated by plagioclase and lesser orthopyroxene and retains layers of garnet and clinopyroxene (Fig. 2a) which commonly form corona (Fig. 2b) around orthopyroxene, aligned with the foliation of the anhydrous rock (Raimbourg *et al.* 2005, Terry & Heidelbach 2006). *P–T* estimates from conventional thermobarometry for the granulitic metamorphic conditions are 10 kbar and 800–900 °C (Austrheim 1987, Boundy *et al.* 1997, Austrheim 2013).

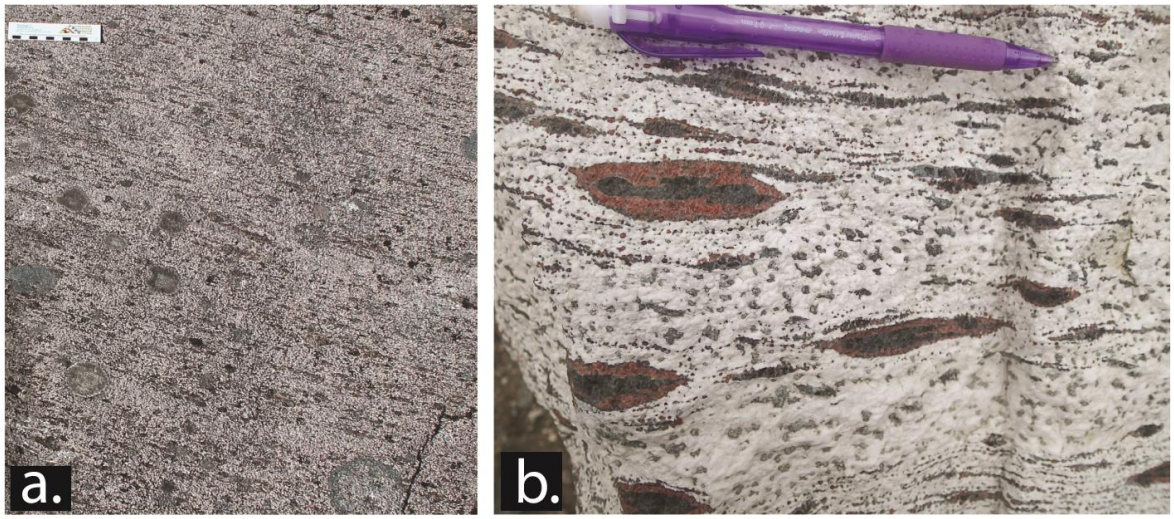

Figure 2. (a) Outcrop of layered anorthositic granulite. (b) Hand sample of coronitic granulite showing the simplified overall mineral reaction plagioclase + orthopyroxene → garnet + clinopyroxene.

The anorthositic granulites were subsequently deeply buried during the Caledonian Orogeny c. 450 Ma (Austrheim & Griffin 1985, Boundy *et al.* 1996, Van Wyck *et al.* 1996) and partially to completely converted to eclogites. The petrology of the eclogites has been described in detail previously (Austrheim & Griffin 1985, Jamtveit *et al.* 1990, Boundy *et al.* 1992, Austrheim *et al.* 1997, Bingen *et al.* 2001, Raimbourg *et al.* 2005, Pollok *et al.* 2008). The essential mineralogy of the eclogites consists of garnet, clinopyroxene and zoisite.

Depending on rock chemical composition, the eclogites may also contain varying amounts of phengite, kyanite, rutile, quartz and amphibole. Previous *P–T* constraints for their formation were based on eclogite parageneses and yielded peak conditions of 15–21 kbar and 650–800 °C, which suggest burial depths of approximately 50–70 km (Austrheim 1987, Jamtveit *et al.* 1990, Boundy *et al.* 1996, Boundy *et al.* 1997, Pollok *et al.* 2008, Austrheim 2013). Later amphibolite-grade reworking of eclogite during exhumation has been interpreted to have occurred at lower *P–T* conditions of 8–12 kbar and 600–700 °C (Boundy *et al.* 1996, Kühn *et al.* 2002). Comparing the ages of the eclogites and amphibolites on Holsnøy (Boundy *et al.* 1992, Kühn *et al.* 2002) with those of the eclogites in the nearby high-pressure Western Gneiss Region (WGR), north of Holsnøy (Tucker *et al.* 1987, Eide *et al.* 1999, Carswell *et al.* 2003, Hacker *et al.* 2010), the data indicate that the rocks of Holsnøy were being exhumed while those of the WGR were being buried.

The transition from granulite to eclogite on Holsnøy has been described by multiple authors (Austrheim 1987, Jamtveit *et al.* 1990, Boundy *et al.* 1992, Boundy *et al.* 1997, Kühn *et al.* 2002, Jolivet *et al.* 2005) and can be seen via different stages of deformation that progressively increase the degree of transformation in the protolith. These stages are explained and depicted, with maps produced by the author, below:

Stage 1: This stage involves the formation of pseudotachylites and discrete fractures with green alteration halos. Pseudotachylites occur in the granulites as pale grey veins and injection structures. They can either cross-cut the foliation of the granulite or follow its trend (Fig. 3a). In most cases, the pseudotachylites are overprinted by the eclogite (Fig. 3a and b). However, in rare instances small injection veins of pseudotachylite cross cut partially modified granulite (Fig. 3c).

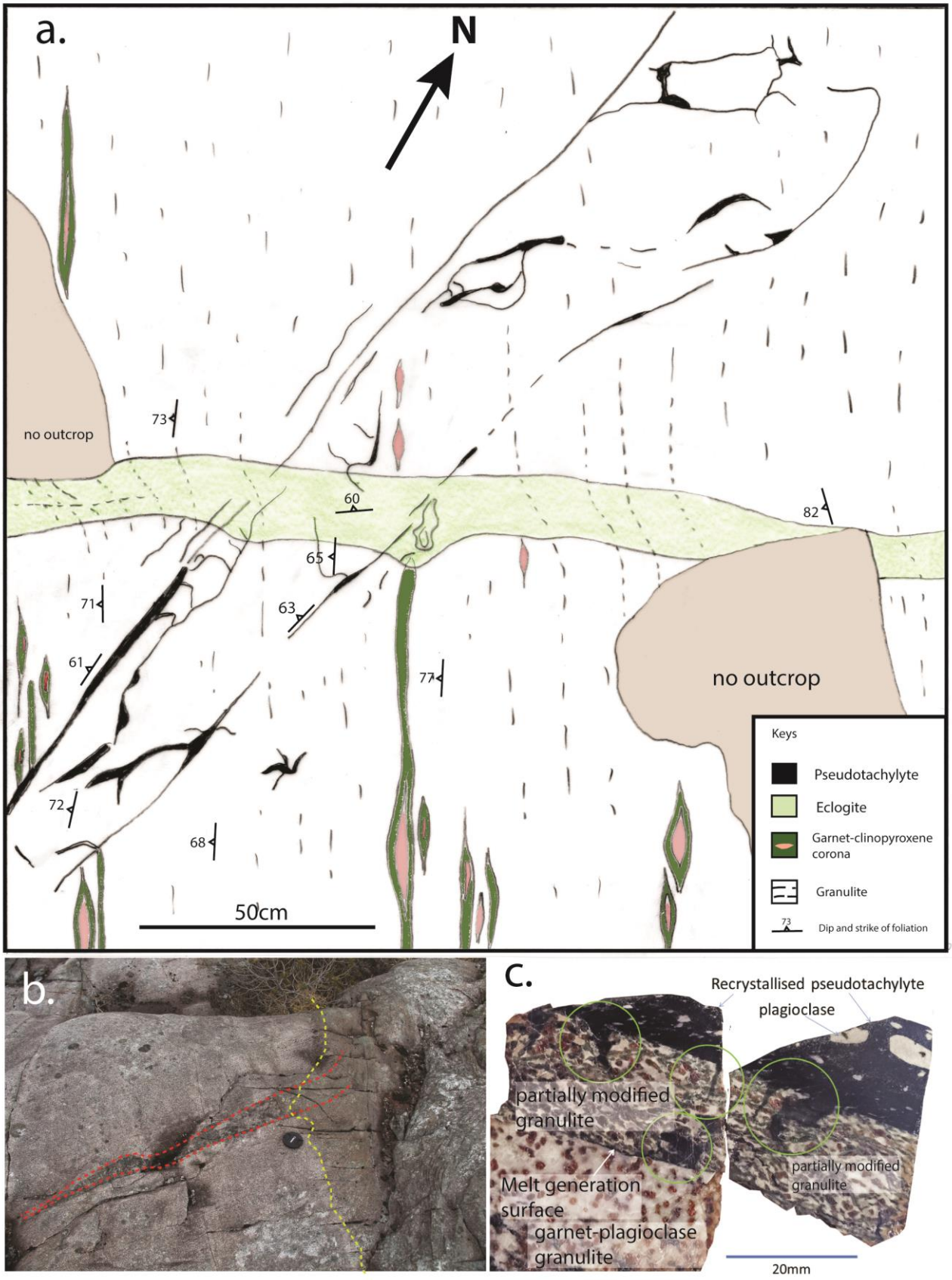

Figure 3. Features of Stage 1 deformation. (a) Detailed map of granulite-hosted pseudotachylite overprinted by eclogite. (b) Pseudotachylite dragged and overprinted by eclogitised shear zone. Red dashed lines outline the pseudotachylite and yellow dashed lines outline the eclogitisedshear zone. (c) Injection veins of pseudotachylite (circled in green) into the partially eclogitised granulite.

Stage 2: This stage involves the formation of discrete shear zones within metasomatised granulite. This is associated with increasing conversion of the granulite (Fig. 4). At this point, the eclogite assemblage generally contains plagioclase which is relict from the protolith. Structurally, the foliation of the granulite is still preserved in the discrete shear zones.

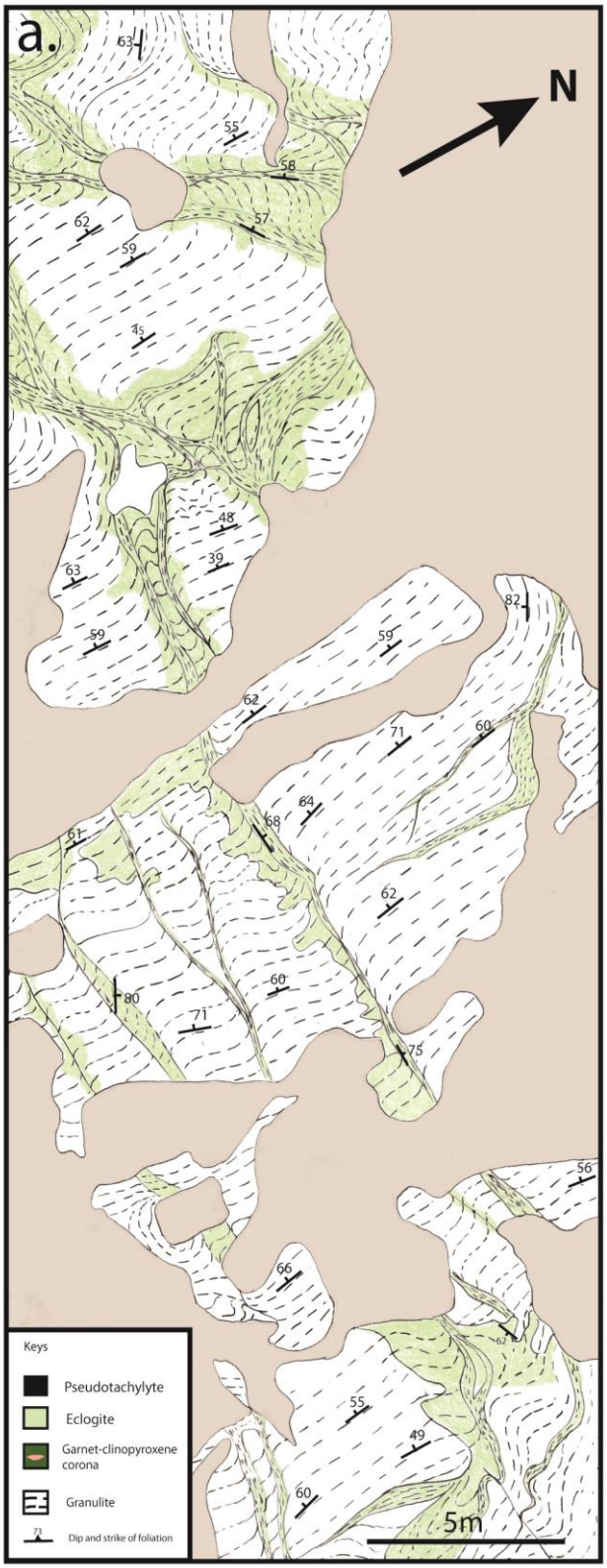

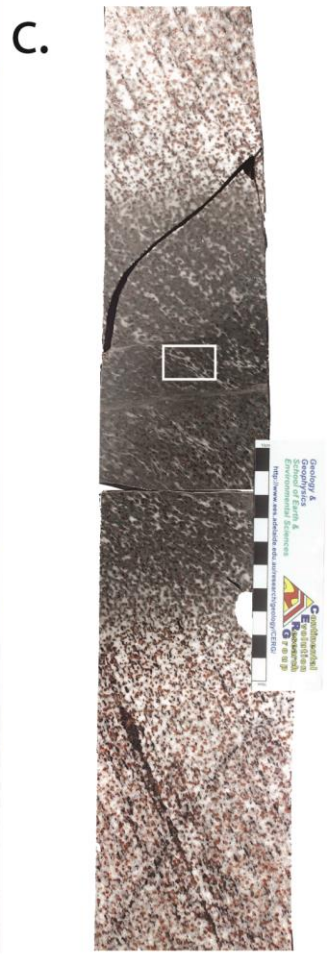

Figure 4. Structural features of Stage 2 of eclogite formation. (a) Detailed map of discrete fractures and shear zones (shaded green) depicting Stage 2 deformation. (b) Field photograph of occurrence of a typical discrete eclogite shear zone (dark green) in granulite. (c) Hand sample of Stage 2 eclogite shear zone overprinting g-cpx-plag granulite. The shear zone is associated with the breakdown of granulite-facies minerals to form fine-grained assemblages which enclose relict garnets. In the granulite, garnet abundance is 18.1%, whereas relict garnet comprises 10.01% of the eclogite shear zone (based on pixel counting using Photoshop). The white square is the location of the thin section shown in Figure 8d.

Stage 3: This stage involves a significant increase in alteration of the granulite. Extensively sheared eclogite forms a ‘matrix’ that encloses some rounded granulite ‘breccia’ with apparent random rotation (Fig. 5a). The granulite blocks vary in size, ranging from metre to tens-of-meter scale, and its foliation usually cannot be traced between adjacent blocks. However, a deflection of the granulite’s fabric into the sheared eclogite’s foliation can be observed at the margins of the granulite blocks attesting to shear deformation in the process of eclogite formation.

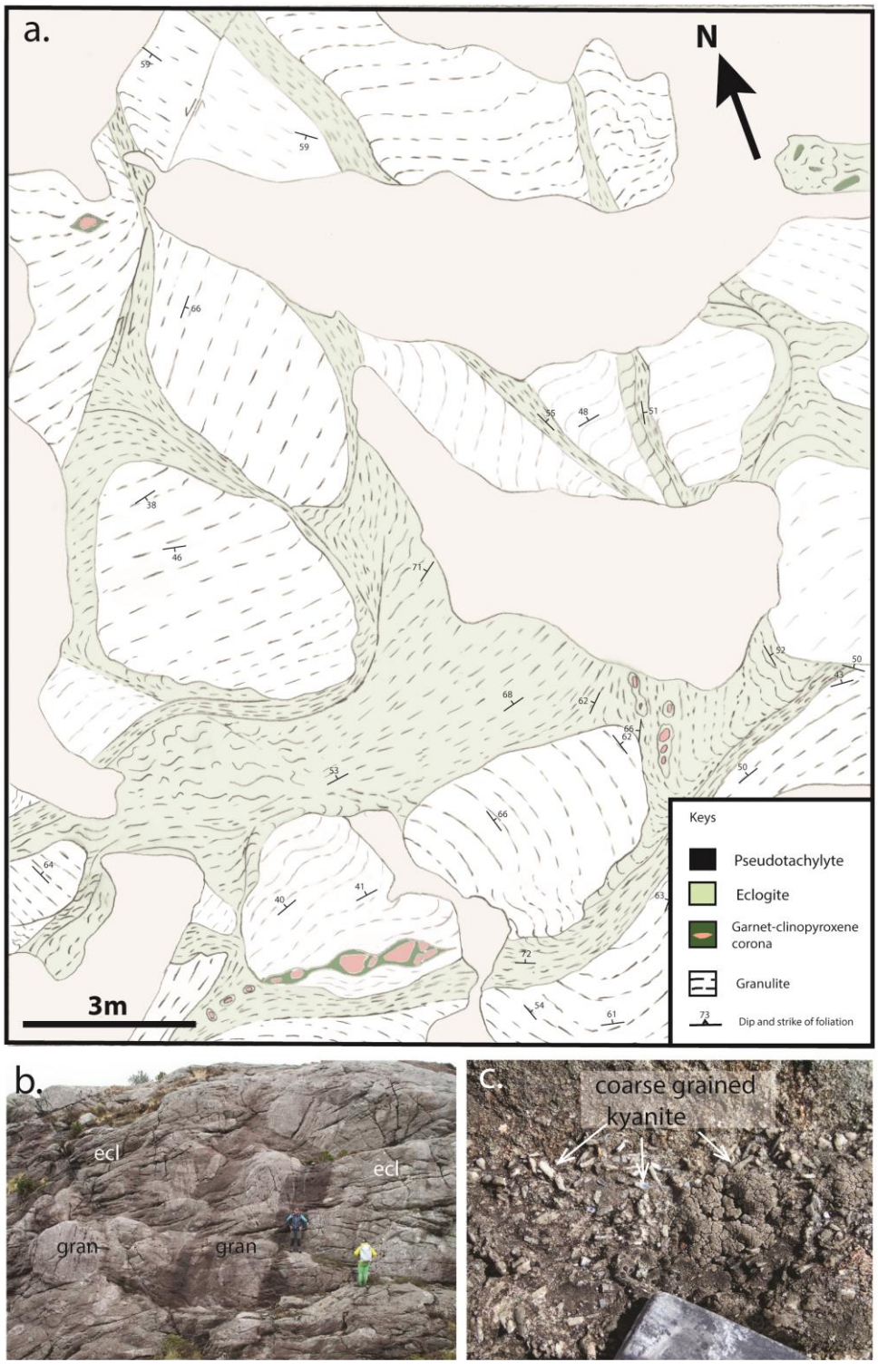

Figure 5. Features in Stage 3 of deformation.(a) Detailed map of granulite ‘breccia’. (b) Field photograph of granulite blocks enclosed in eclogite. (c) Outcrop of part of the extensively sheared eclogite showing coarse-grained kyanite.

Stage 4: This stage is essentially the complete replacement of the granulite at scales greater than 50 m (Fig. 6a). Stage 4 domains are organized into deformation belts that principally trend at about 110/20NE, with a subordinate conjugate that trends 050/20SE. Within the ESE trending eclogite belts, relict granulite occurs as blocks with diffuse margins that commonly have sigmoidal shapes (Fig. 6a), suggesting bulk dextral top-to-the-east non-coaxial flow within the eclogite deformation belts (Jolivet *et al.* 2005, Raimbourg *et al.* 2005). Figure 6d shows a generalised structural model for the development of the eclogite shear system on Holsnøy.

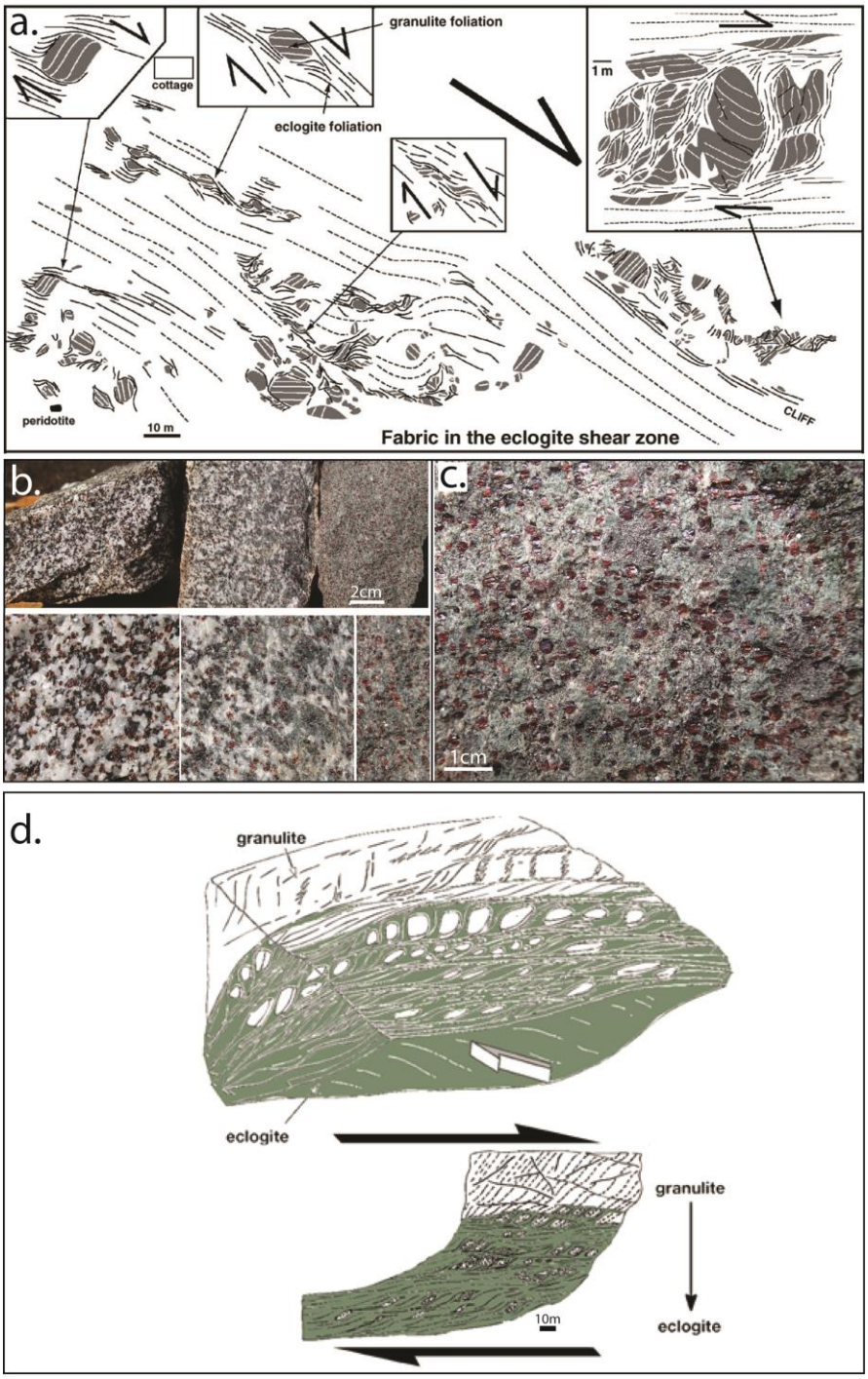

Figure 6. Modified from Jolivet *et al* (2005) showing models depicting processes in Stage 4 of deformation. (a) Remnants of granulite within the pervasive eclogite. Insets show details of metre-scale kinematic indicators. (b) Hand samples showing the transition from granulite to partially eclogitised domains. (c) Hand specimen of eclogite fully converted from granulite. (d) Schematic interpretation of the progressive deformation of the Holsnøy granulite during top-to-the-east shear. 3D sketch of transition from fresh granulite (white) to eclogite shear zone (green).

Stage 5: In places the eclogite has been overprinted by localized, coarse-grained muscovite-bearing domains (Fig. 7a), in which muscovite-poor eclogite is broken into fragments (Fig. 7b). These domains contain euhdreal garnet and disseminated clinopyroxene and amphibole. These muscovite-rich domains may form the early stages of the amphibolite facies overprint that occurred during exhumation of the eclogites (Boundy *et al.* 1992, Kühn *et al.* 2002)

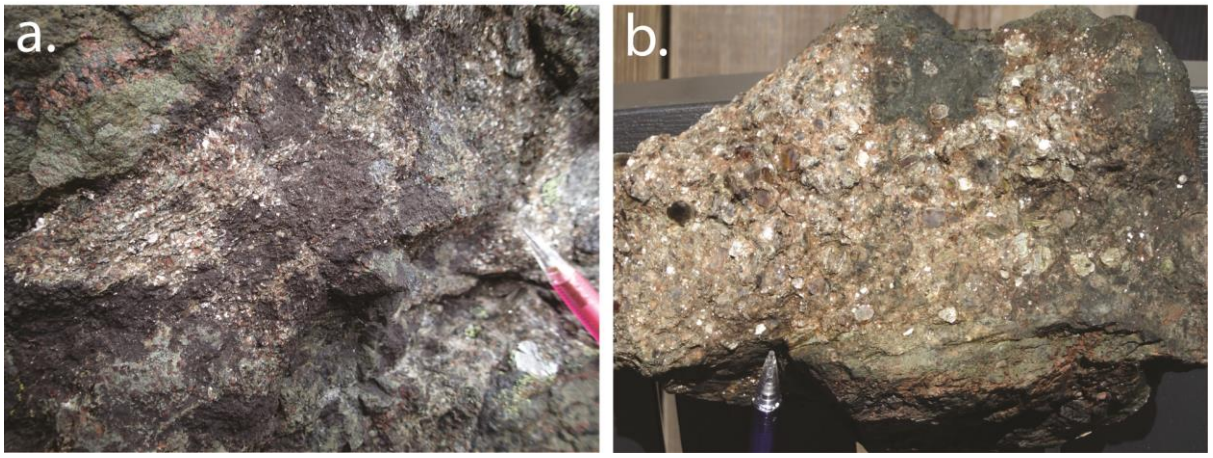

Figure 7. Retrogressive muscovite-rich eclogite formed during Stage 5 of deformation. (a) Field photograph of muscovite schist. (b) Sample showing eclogite (pale and dark green) from Stage 4 partially retrogressed by the golden–silvery muscovite schist.

3. METHODS

3.1. Detailed mapping and sample collection

Detailed outcrop-scale mapping (Figs. 3a, 4a and 5a) was undertaken on Holsnøy in May 2015 to document the progressive conversion of the granulite to eclogite. Mapping was done using gridded outcrop, with grid size determined by the scale needed to show the essential features of each structural stage.

Samples for petrological forward modelling were then collected within the framework of the deformation stages. The aim of sampling was to identify the rocks that had essentially completely recrystallised during different stages of the deformation history.

3.2. Bulk-rock and mineral chemistry

Whole-rock geochemistry for implementation in phase equilibria forward modelling was done at the Department of Earth and Environment, Franklin and Marshall College, Lancaster PA, using Wavelength Dispersive X-ray Fluorescence (WD–XRF) spectrometry. Major elements were analysed on fused disks prepared using a lithium tetraborate flux. Ferric vs ferrous iron content was determined by wet chemistry methods.

Mineral composition element analyses and element X-ray maps were acquired using a CAMECA SXFive electron microprobe at Adelaide Microscopy, University of Adelaide. For elemental analyses, a beam current of 20 nA and accelerating voltage of 15 kV was used. Prior to analysis, calibration was done on the Andradite standard crystal, and Wavelength Dispersive Spectrometers (WDS) were used for the analysis of SiO_2, ZrO_2, TiO_2, ZnO, Al_2O_3, Cr_2O_3, FeO, MnO, MgO, CaO, BaO, Na_2O, K_2O, P_2O, Cl, F and O. Element maps for all samples were done using a beam current of 200 nA and accelerating voltage of 15 kV. Step sizes and dwell times were chosen based on the size of the area mapped and the grain size of the minerals to maximise the resolution. Elements Ca, Fe, Mn and Mg were mapped using WDS, and Al, Si, Ti, K, Na, Zr, Cl, Ce and F were mapped using Energy Dispersive Spectrometers (EDS).

3.3. Phase equilibria forward modelling

3.3.1. BULK-ROCK COMPOSITION DETERMINATION

Bulk compositions for phase[1] equilibria forward modelling using THERMOCALC were recast in terms of mole percentage of oxide components (e.g. MgO, SiO_2, etc.) from the weight percent data in whole-rock geochemical analyses. For samples that had completely recrystallised, the forward modelling calculations used the recast values directly from XRF

[1] phase, rather than mineral, is used in the context of thermodynamic modelling. The term ‘mineral’ is reserved for the naturally occurring material.

and wet chemistry analyses. However, for samples that still contained relicts from the granulitic mineralogy, it was necessary to derive an effective reactive bulk composition prior to using the forward modelling software. This was done by determining the proportion of relict mineralogy and its composition from the electron microprobe data and then subtracting that compositional reservoir from the whole rock geochemical analysis.

3.3.2. PRESSURE–TEMPERATURE PSEUDOSECTIONS

Phase equilibria calculations were undertaken using the software programs THERMOCALC v.3.33 and Perple_X (Holland & Powell 1998, Connolly & Petrini 2002, Connolly 2005, Holland & Powell 2011) in the geologically-realistic chemical system MnO–Na_2O–CaO–K_2O–FeO–MgO–Al_2O_3–SiO_2–H_2O–TiO_2–O, where 'O' is a proxy for Fe_2O_3, using the internally-consistent thermodynamic dataset 'ds5' (filename ds55.txt, 22nd Nov 2003 update of Holland & Powell, 1998). The activity–composition (*a–x*) models used were: amphibole (Diener *et al.* 2007, Diener & Powell 2012); clinopyroxenes (Green *et al.* 2007, Diener & Powell 2012); chlorite (Holland & Powell 1998); garnet (White *et al.* 2007); epidote–clinozoisite (Holland & Powell 1998); plagioclase (Holland & Powell 2003); K-feldspar (Holland & Powell 2003); ilmenite (White *et al.* 2000); muscovite and paragonite (Coggon & Holland 2002); chloritoid (White *et al.* 2000) and talc (Holland & Powell 1998).

Forward models were first calculated in Perple_X as a reconnaissance tool to provide a guide for what the phase relationships might look like in *P–T* space, before beginning the more complicated task of calculating phase diagrams in THERMOCALC. Calculations in Perple_X are based on Gibbs energy minimisation over a user-specified gridded *P–T* or *T–X* range. Perple_X is automated software which requires only the bulk-rock composition in weight percentage, the list of solid-solution phases to be used by the calculation process, the name of the thermodynamic dataset file and the *P–T* range.

Calculations in THERMOCALC are based on the user specifying the stable assemblage and calculating each and every field boundary and intersection of field boundaries, where field boundaries (lines) represent zero abundance of a phase and intersections (points) represent zero abundance of two phases. The initial stable assemblage is determined by performing a Gibbs energy minimisation calculation at a set pressure–temperature (*P–T*) condition. The model is built up and around from that initial assemblage and involves a large number of trial and error calculations in order to determine which phases appear or disappear as a function of pressure, temperature and/or composition (*X*). In addition, the so-called 'starting guesses' (values for compositional variables with which THERMOCALC commences its iterative least-squares calculation for a field boundary or intersection) require regular updating as the model is calculated in different parts of *P–T–X* space. A single model usually comprises of more than 150–200 total line and intersection calculations and typically takes several weeks to calculate and construct.

3.3.3. CONTOURS OF PHASE CHEMISTRY

Contouring of forward models for the compositions and abundances ('mode') of phases was calculated using the Matlab-based, automated software TCInvestigator v1.1 (Pearce *et al.* 2014). In addition to the THERMOCALC input files and executable (.exe) files, the finished *P–T* model from THERMOCALC and an additional 'assemblage' file are required as input to TCInvestigator. The 'assemblage' file must list phase assemblages in the same order as used for shading/colouring the *P–T* model, which is based on the variance of each phase assemblage field.

4. RESULTS

4.1. Petrography

Four samples were chosen to encompass the structural evolution (see Section 2.3)

- Sample HOL2A_2015 is from a vein of recrystallised pseudotachylite within the granulite-dominated domain and is an example of Stage 1 deformation (Section 2.3). Phase equilibria modelling were done on this sample to constrain the *P*–*T* conditions on the prograde path.
- HOL4A_2014 is from the transitional stage of granulite to eclogite (Stages 2 and 3). Owing to the significant preservation of granulitic relicts in these samples, they were not used for phase equilibria forward modelling.
- Sample HOL7C_2014 is from the pervasive eclogite (Stage 4). It contained relict garnet inherited from the precursor granulite and modification of its whole-rock composition was necessary in order to remove relict garnet and calculate an applicable forward model.
- Sample HOL13C_2015 is a coarse-grained, muscovite-rich domain which developed at the interface between granulite and eclogite within the overall transitional Stage 3 to 4. The sample is pervasively foliated muscovite schist representative of Stage 5 and contains small garnet and sodic clinopyroxene (i.e. omphacite) crystals. It overprints the earlier muscovite-poor eclogite which occurs as small boudins within the schist. Phase equilibria modelling were done for this sample to constrain the *P*–*T* conditions on the retrograde path.

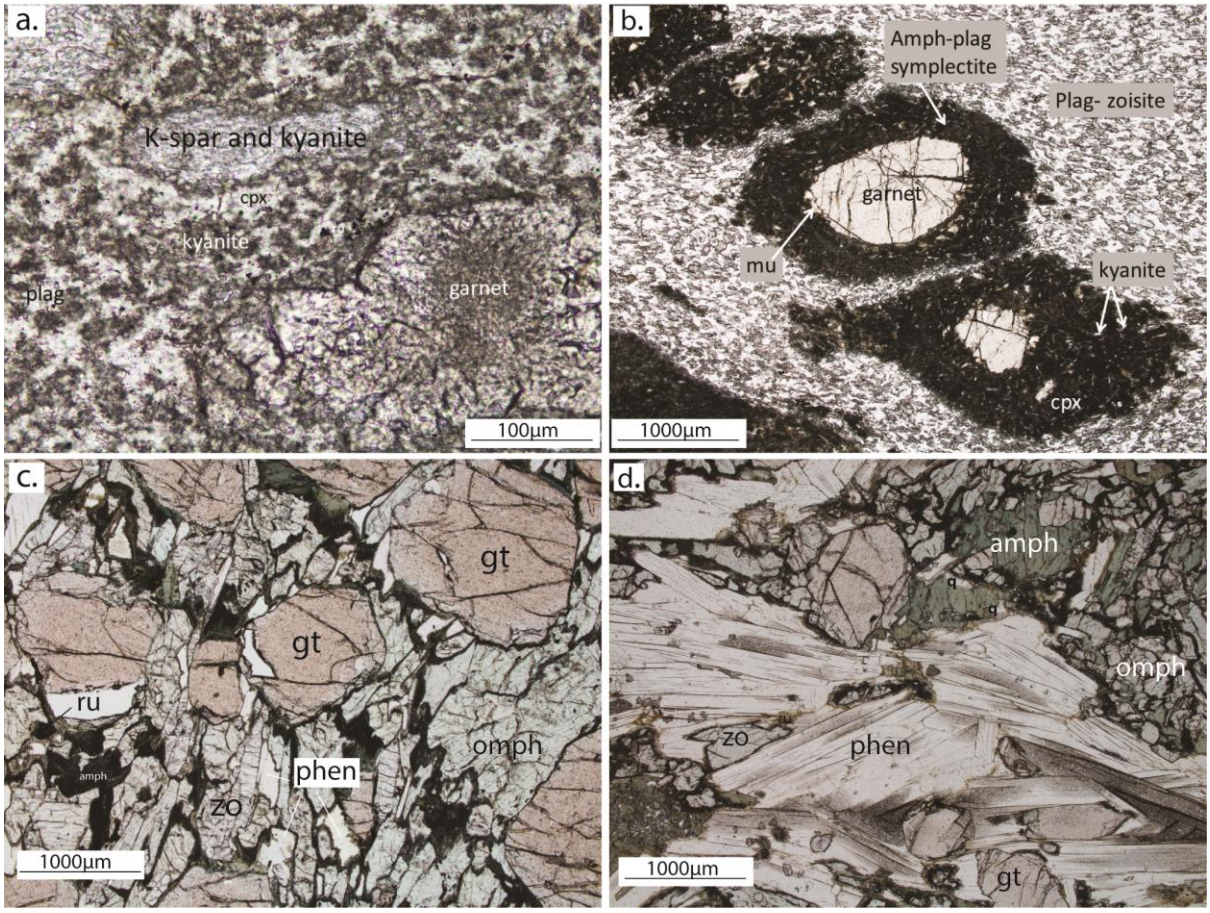

Figure 8. Photomicrographs showing the textures of the eclogites and the mineralogical relationship. (a) HOL2A is the recrystallised pseudotachylite from Stage 1 of deformation. The matrix comprises very fine grained intergrowth of light-colour plagioclase and clinopyroxene and darker coloured kyanite enclosing K-feldspar and kyanite growth, which adopts a particular lense shape, and few garnet poikiloblasts . (b) HOL4A is the sample representing Stages 2 and 3. Relict granulitic garnet grains are enclosed by fine-grained amphibole-plagioclase-bearing symplectites and kyanite, omphacite and muscovite completely replaces garnet. The light-coloured matrix comprises of plagioclase and zoisite. (c) HOL7C occurs in Stage 4 deformation. Garnet with apparent zoning sits in a matrix of omphacite, zoisite and phengite with growth of amphibole-rich symplectites at garnet-omphacite grain boundaries. (d) HOL13A is from Stage 5 of deformation. Coarse-grained phengite matrix breaks down amphibole-omphacite-zoisite-garnet-quartz-bearing domains into isolated aggregates.

HOL2A_2015

This sample is from a recrystallised pseudotachylite vein that cuts the granulite fabric. The rock has a fine-grained (<0.1 mm) matrix (Fig. 8a) comprising kyanite, clinopyroxene, plagioclase, K-feldspar and minor amounts of quartz, magnetite and rutile. Coarse-grained scapolite (up to 1mm) rarely occurs in the matrix. Small clusters of kyanite needles occur intergrown with clinopyroxene (Fig. 8a). The matrix also contains domains of intergrown K-feldspar and kyanite (1–2 mm; Fig. 8a). Within these domains the kyanite is weakly aligned defining an incipient foliation in the rock; however, kyanite in the matrix enclosing the K-

feldspar–kyanite domains is not foliated. Garnet occurs in minor amounts, and occurs as highly poikiloblastic grains (0.2– 0.25 mm; Fig. 8a) that contain inclusions of plagioclase, K-feldspar, quartz, clinopyroxene and minor magnetite and rare rutile and calcite. The rims of the garnet tend to have fewer inclusions. The peak metamorphic assemblage of the recrystallised pseudotachylite is garnet–kyanite–plagioclase–K-feldspar–omphacite–zoisite/clinozoisite–scapolite ± quartz.

HOL4A_2014

The sample comes from within a Stage 2 ductile shear zone. It contains a well-developed foliation defined by zoisite that is set within a recrystallised plagioclase matrix (Fig. 8b). The zoisite–plagioclase domains enclose relict garnet (Fig. 8b) inherited from the granulite and there are well-developed symplectites consisting of extremely fine-grained amphibole and plagioclase (Fig. 8b). These symplectites are not foliated, and are interpreted to have formed subsequent to deformation. Within the symplectites are rare, coarse-grained domains that contain kyanite, clinopyroxene and minor phengite (muscovite with a Mg and an Fe component; Table 4) (Fig. 8b). In places the fine-grained symplectites directly mantle kyanite and clinopyroxene. The kyanite–clinopyroxene–phengite-bearing domains are interpreted to have initially replaced garnet, forming part of a mineral assemblage consisting of zoisite–plagioclase–clinopyroxene–kyanite–phengite.

HOL7C_2014

This sample contains a well-defined foliation consisting of zoisite, elongate clinopyroxene (omphacite) and phengite (Fig. 8c). The foliation encloses garnets which have subtle colour variation from relatively pink cores to lighter rims (see top right of Fig. 8c). Relatively scarce rutile occurs within the foliated matrix. X-ray mapping revealed the presence of rare Si and Al–Si grains which confirmed the presence of minor quartz and kyanite, respectively. Phengite, clinopyroxene and garnet are usually rimmed with small, dark, fine-grained symplectites consisting of green–blue amphibole, albitic plagioclase and zoisite (Fig. 8c). The symplectites are typically better formed at grain boundaries that occur at a high angle to the foliation. This suggests that symplectites may have developed during later stages of the deformation that produced the foliation. The interpreted peak metamorphic assemblage for HOL7C_2014 is phengite–garnet–rutile–kyanite–zoisite–omphacite.

HOL13A_2015

HOL13A_2015 is from the muscovite-rich schist overprinting the completely eclogitised domains, formed in Stage 5. The sample contains medium-grained (0.2–1 mm) garnet, omphacite, zoisite, green amphibole and quartz, which are all into contact along grain boundaries. These minerals form aggregates which are isolated by very coarse phengite grains (1–3 mm; Fig. 8d). The interpreted peak metamorphic assemblage is phengite–garnet–omphacite–rutile–amphibole–quartz–zoisite. The sample has poor foliation and phengite grains grow at high angles to each other. Relative abundance of each minerals is as follow: 35 % phengite; 15 % amphibole; 5% zoisite; 3–4 % quartz; 15 % omphacite; 15 % garnet; 5 % rutile.

4.2. Whole-rock geochemistry and Mineral chemistry

Table 1 is a summary of whole-rock compositions expressed as weight percent (wt %) for the samples modelled using THERMOCALC and Table 2 is a summary of the mole percent (mol %) values input in THERMOCALC.

Table 1. Bulk-rock composition of chosen samples for phase modelling expressed in wt %.

Sample	HOL2A_2015 (Stage 1)	HOL4C_2014 (Stages 2)	HOL7C_2014 (Stage 4)	HOL13A_2015 (Stage 5)
SiO2	50.81	50.54	46.51	48.33
TiO2	0.08	0.10	0.61	0.64
Al2O3	24.72	24.92	18.65	20.69
Fe2O3T	4.52	5.40	11.39	9.54
MnO	0.09	0.07	0.20	0.21
MgO	4.72	5.49	6.60	7.10
CaO	10.02	8.54	10.93	7.70
Na2O	4.06	3.92	3.34	3.02
K2O	0.57	0.45	0.79	2.49
P2O5	0.07	0.03	0.03	0.04
LOI	0.91	0.74	1.36	2.44
FeO	2.80	3.68	7.23	6.22
Fe2O3	1.41	1.31	3.35	2.63
Total	**99.66**	**99.79**	**99.60**	**99.76**

*HOL4C_2014 was not modelled as it is only partially modified.

Table 2. Un-normalised bulk-rock composition in the system NCKFMASHTO expressed in mol % as input to THERMOCALC.

Sample	HOL2A_2015 (Stage 1)	HOL7C*_2014 (Stage 4)	HOL7C_2014 (Stage 4)	HOL13C_2015 (Stage 5)
SiO2	54.39	48.91	48.55	48.98
TiO	0.06	0.48	0.53	0.49
Al2O3	15.59	11.56	10.88	12.35
FeO*	3.64	9.01	6.87	7.28
MgO	7.53	10.35	9.15	10.73
CaO	11.49	12.31	12.84	8.36
Na2O	4.21	3.4	3.85	2.97
K2O	0.39	0.53	0.6	1.61
H2O	3.25	4.77	5.39	8.25
O	0.57	1.33	1.35	1

HOL7C* designates the original bulk composition for this sample (including relict garnet inherited from the granulitic protolith) whereas HOL7C is the modified bulk composition derived from removing the relict granulitic garnet from the whole-rock composition. The composition of the relict garnet is on the basis of electron micrprobe-measured mineral composition data(see Table 3).
FeO* = $FeO_{(original)}$ + 2×O as 'O' specifies the amount of excess oxygen required to oxidise FeO to create Fe_2O_3.

Garnet grains in sample HOL7C_2014 (Stage 4) have well defined rims (optically and compositionally). These are most evident in the elemental X-ray map for Ca (Fig. 9a) and to a lesser extent in the iron (Fig. 9b) and magnesium (Fig. 9c) maps. The garnet rims are compositionally rich in calcium but depleted in magnesium relative to the compositionally homogeneous core (Fig. 9). Figure 10 shows a quantitative compositional traverse across the garnet shown in Figure 9. The rims (pink shading in Fig. 10) are interpreted to have formed during eclogite-facies metamorphism whereas the garnet cores of distinctly different composition (purple shading in Fig. 10) are interpreted as inherited from the granulitic protolith. Spinel inclusions in some of the lower-Ca garnet cores support the interpretation of a granulitic origin. The abundance of granulitic garnet calculated from the Ca map (Fig. 9a) was determined to be 75.8%. This information was combined with the quantitative composition of granulitic garnet (Fig. 10) to subtract it from the whole-rock composition for *P–T* modelling.

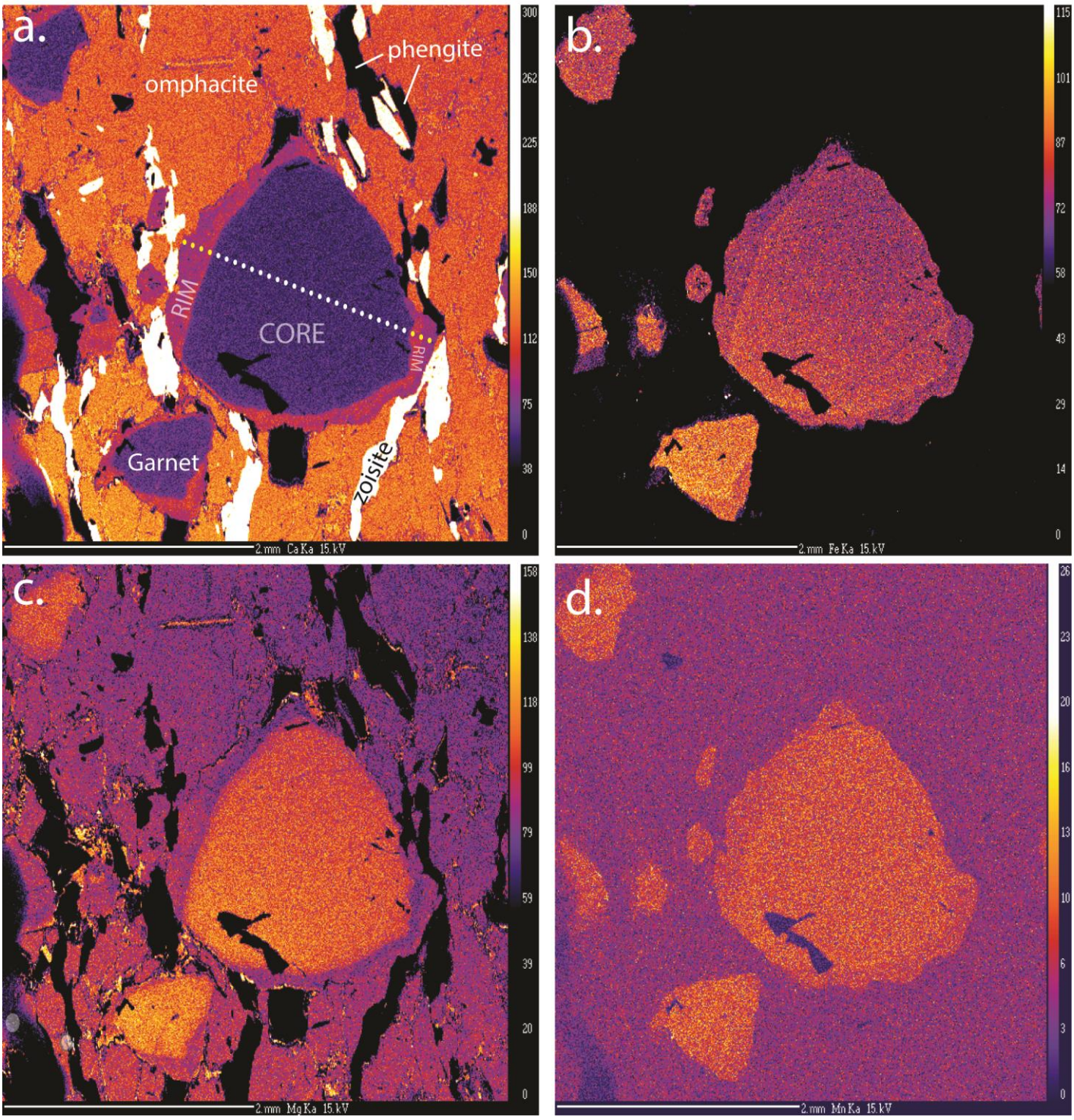

Figure 9. Electron microprobe X-ray elemental maps for HOL7C_2014. (a) Calcium map: The spots defining a traverse indicate where electron microprobe analyses (Table 2) were made. Yellow spots/analyses are on the higher-Ca, eclogitic rim of the garnet whereas white spots/analyses are on the lower-Ca, granulitic core. (b) Iron map. (c) Magnesium map. (d) Manganese map.

Table 3. Representative elemental analyses of garnet (Fig. 9) in HOL7C_2014, expressed in wt %. Core values were almost constant; therefore they are given as a range.

	Rim				Core	Rim		
SiO2	38.82	38.39	38.55	38.59	38.54-39.23	38.95	38.91	38.90
TiO2	0.03	0.05	0.12	0.19	0.07-0.17	0.14	0.06	0.04
Al2O3	21.87	21.58	21.86	21.56	21.24-21.59	21.69	21.90	21.94
Cr2O3	0.05	0.03	0.01	0.01	0.00-0.03	0.04	0.00	0.03
FeO	21.61	21.90	21.99	21.65	22.61-23.58	21.70	21.85	21.82
MnO	0.48	0.53	0.41	0.39	0.66-0.77	0.50	0.44	0.52
MgO	8.13	8.03	7.86	6.80	9.40-10.33	7.81	8.07	8.25
ZnO	0.00	0.00	0.00	0.00	0.00-0.03	0.05	0.00	0.00
CaO	8.57	8.37	8.87	10.33	5.42-5.91	8.99	8.56	8.76
Na2O	0.01	0.02	0.05	0.06	0.00-0.03	0.03	0.02	0.01
K2O	0.00	0.02	0.00	0.00	0.00-0.01	0.00	0.00	0.01
Cl	0.01	0.01	0.00	0.01	0.00-0.01	0.00	0.00	0.01
F	0.00	0.01	0.01	0.00	0.00-0.07	0.03	0.00	0.01
Total	99.58	98.93	99.73	99.59	97.94-101.60	99.92	98.81	100.29
Cations								
Si	2.97	2.96	2.95	2.97	2.95-2.98	2.98	2.97	2.96
Ti	0.00	0.00	0.01	0.01	0.00-0.01	0.01	0.00	0.00
Al	1.97	1.96	1.97	1.96	1.91-1.94	1.96	1.97	1.97
Cr	0.00	0.00	0.00	0.00	0	0.00	0.00	0.00
Fe3+	0.08	0.10	0.11	0.09	0.11-0.17	0.06	0.07	0.11
Fe2+	1.31	1.31	1.30	1.31	1.29-1.36	1.32	1.32	1.28
Mn2+	0.03	0.03	0.03	0.03	0.04-0.05	0.03	0.03	0.03
Mg	0.93	0.92	0.90	0.78	1.07-1.17	0.89	0.92	0.94
Zn	0.00	0.00	0.00	0.00	0	0.00	0.00	0.00
Ca	0.70	0.69	0.73	0.85	0.44-0.48	0.74	0.70	0.71
Na	0.00	0.00	0.01	0.01	0	0.00	0.00	0.00
K	0.00	0.00	0.00	0.00	0	0.00	0.00	0.00
Cl	0.00	0.00	0.00	0.00	0	0.00	0.00	0.00
F	0.00	0.00	0.00	0.00	0.00-0.02	0.01	0.00	0.00
Total	8.00	8.00	8.00	8.00	8	8.00	8.00	8.00
End-members								
p(alm)	0.46	0.46	0.46	0.46	0.47-0.49	0.46	0.46	0.45
p(py)	0.31	0.30	0.29	0.26	0.35-0.38	0.29	0.30	0.31
p(grs)	0.23	0.23	0.24	0.28	0.14-0.15	0.24	0.23	0.23
p(spss)	0.01	0.01	0.01	0.01	0-0.02	0.01	0.01	0.01

Analysis locations were equidistant along a traverse (Fig. 9a). p(alm), p(py), p(gros), p(spss) are the proportions of the different garnet end-members; almandine, pyrope, grossular and spessartine, respectively.

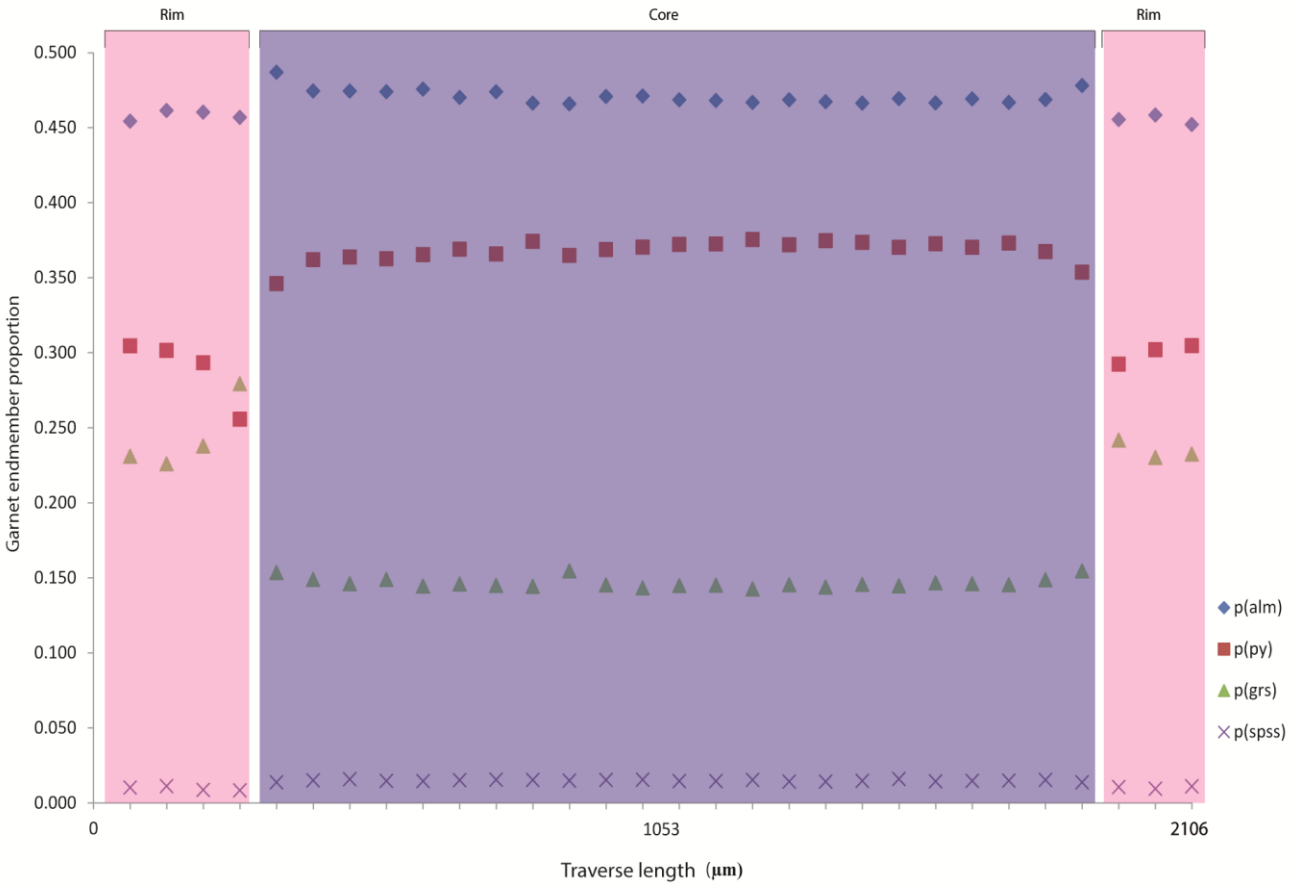

Figure 10. Compositional profile across garnet (rim to core to opposite rim) shown in Fig. 9 in sample HOL7C_2014. There is a clear discontinuity in the Fe (blue diamonds), Mg (red squares) and Ca (green triangles) content of garnet towards the rim, highlighted by change from purple to pink shading on plot. Compositional data for the plot is from Table 3.

Phengite–white mica compositions (Table 4) vary from around 8% to 16% paragonite component based on the amount of Na_2O. The phengite (Fe–Mg) component comprises approximately 33–37% of the white mica composition and the remainder is comprised of the muscovite component (approximately 44–58%). Omphacite compositions (Table 5) comprise an approximate 37–41% jadeite component, approximately 8–13% aegerine (Fe^{3+} clinopyroxene) component, 0–7% hedenbergite component and the remainder comprises the diopside component (approximately 44–50%).

Table 4. Representative compositional analyses of phengitic (Fe–Mg-bearing) muscovite in HOL7C_2014 expressed in wt %. The deficit in wt% total is due to the presence of volatiles (e.g. water) in white mica.

	Phengitic muscovite									
SiO2	46.75	46.87	47.67	46.88	47.04	46.54	47.20	46.85	47.11	47.40
ZrO2	0.00	0.00	0.02	0.06	0.00	0.07	0.00	0.00	0.00	0.02
TiO2	0.75	0.78	0.76	0.78	0.73	0.70	0.75	0.77	0.74	0.75
ZnO	0.00	0.00	0.00	0.00	0.00	0.00	0.00	0.00	0.00	0.00
Al2O3	31.86	31.54	31.82	31.26	31.53	32.21	31.41	30.93	31.21	31.04
V2O3	0.05	0.06	0.03	0.02	0.05	0.05	0.03	0.05	0.05	0.03
Cr2O3	0.05	0.00	0.00	0.00	0.00	0.00	0.00	0.00	0.00	0.02
FeO	1.75	1.85	1.85	1.91	1.94	1.89	2.01	2.04	1.98	2.01
MnO	0.00	0.00	0.00	0.01	0.02	0.01	0.00	0.00	0.00	0.01
MgO	2.40	2.48	2.51	2.55	2.50	2.34	2.58	2.49	2.42	2.58
CaO	0.00	0.02	0.01	0.01	0.01	0.02	0.03	0.01	0.00	0.02
BaO	1.01	1.03	0.96	0.98	0.98	0.98	0.97	0.98	1.00	0.97
Na2O	1.13	1.22	1.29	1.43	1.32	0.64	0.81	1.22	1.10	1.51
K2O	8.47	8.16	8.07	8.22	7.94	8.70	8.15	7.98	8.22	7.74
Total	94.21	94.01	94.99	94.12	94.05	94.15	93.96	93.31	93.83	94.09
Cations										
Si	3.164	3.176	3.189	3.179	3.182	3.154	3.193	3.196	3.197	3.203
Ti	0.038	0.040	0.038	0.040	0.037	0.036	0.038	0.040	0.038	0.038
Al	2.541	2.519	2.509	2.498	2.513	2.572	2.504	2.487	2.496	2.472
Cr	0.003	0.000	0.000	0.000	0.000	0.000	0.000	0.000	0.000	0.001
Fe2+	0.099	0.105	0.103	0.108	0.110	0.107	0.114	0.116	0.112	0.114
Mn2+	0.000	0.000	0.000	0.001	0.001	0.001	0.000	0.000	0.000	0.001
Mg	0.242	0.251	0.250	0.258	0.252	0.236	0.260	0.253	0.245	0.260
Zn	0.000	0.000	0.000	0.000	0.000	0.000	0.000	0.000	0.000	0.000
Ca	0.000	0.001	0.001	0.001	0.001	0.001	0.002	0.001	0.000	0.001
Na	0.148	0.160	0.167	0.188	0.173	0.084	0.106	0.161	0.145	0.198
K	0.731	0.705	0.689	0.711	0.685	0.752	0.703	0.694	0.712	0.667
Total	7	7	7	7	7	7	7	7	7	7
End-members										
n(mu) = p(pa, Na)	0.15	0.16	0.17	0.19	0.17	0.08	0.11	0.16	0.14	0.20
c(mu) = p(ma, Ca)	0.00	0.00	0.00	0.00	0.00	0.00	0.00	0.00	0.00	0.00
p(mu)	0.51	0.48	0.48	0.44	0.46	0.57	0.52	0.47	0.50	0.43
p(cel)	0.24	0.25	0.25	0.26	0.25	0.24	0.26	0.25	0.24	0.26
p(fcel)	0.10	0.10	0.10	0.11	0.11	0.11	0.11	0.12	0.11	0.11

Analysis was performed on phengitic muscovite grains shown in Fig. 9a. n and c are the compositional variable Na and Ca, respectively, as defined in the *a-x* model for white mica in THERMOCALC. p(mu), p(cel) and p(fcel) are the proportion of each of the white mica end-member.

Table 5. Representative compositional analyses of omphacite in HOL7C_2014 expressed in wt %.

	Omphacite									
SiO2	53.87	54.02	53.62	53.97	53.93	54.12	54.22	54.55	54.62	54.43
ZrO2	0.03	0.00	0.00	0.00	0.03	0.03	0.00	0.00	0.04	0.00
TiO2	0.23	0.22	0.18	0.17	0.18	0.18	0.18	0.17	0.18	0.18
ZnO	0.05	0.00	0.07	0.00	0.00	0.05	0.04	0.06	0.02	0.00
Al2O3	12.06	11.72	11.33	11.41	11.49	11.75	11.78	11.94	11.66	11.44
V2O3	0.04	0.05	0.02	0.07	0.07	0.04	0.04	0.02	0.06	0.08
Cr2O3	0.01	0.04	0.00	0.00	0.02	0.01	0.00	0.01	0.03	0.00
FeO	5.43	5.49	5.42	5.37	5.57	5.30	5.19	5.25	5.29	5.28
MnO	0.02	0.02	0.01	0.01	0.03	0.02	0.00	0.02	0.03	0.01
MgO	7.99	8.09	8.04	8.25	8.15	8.08	7.93	8.04	8.12	8.33
CaO	13.15	13.22	13.25	13.03	13.05	12.98	12.82	12.66	12.90	12.97
BaO	0.01	0.01	0.00	0.00	0.00	0.00	0.00	0.01	0.00	0.00
Na2O	6.95	6.77	7.01	7.17	7.17	6.95	7.36	7.05	6.96	6.94
K20	0	0	0	0	0	0	0	0	0	0
Total	99.83	99.65	98.96	99.44	99.68	99.53	99.57	99.77	99.92	99.64
Cations										
Si	1.94	1.95	1.95	1.95	1.95	1.95	1.95	1.96	1.96	1.96
Ti	0.01	0.01	0.00	0.00	0.00	0.00	0.00	0.00	0.00	0.00
Al	0.51	0.50	0.49	0.49	0.49	0.50	0.50	0.50	0.49	0.48
Cr	0.00	0.00	0.00	0.00	0.00	0.00	0.00	0.00	0.00	0.00
Fe2+	0.16	0.17	0.16	0.16	0.17	0.16	0.16	0.16	0.16	0.16
Mn2+	0.00	0.00	0.00	0.00	0.00	0.00	0.00	0.00	0.00	0.00
Mg	0.43	0.43	0.44	0.44	0.44	0.43	0.43	0.43	0.43	0.45
Zn	0.00	0.00	0.00	0.00	0.00	0.00	0.00	0.00	0.00	0.00
Ca	0.51	0.51	0.52	0.50	0.50	0.50	0.49	0.49	0.50	0.50
Na	0.48	0.47	0.49	0.50	0.50	0.49	0.51	0.49	0.48	0.48
K	0.00	0.00	0.00	0.00	0.00	0.00	0.00	0.00	0.00	0.00
Total	4	4	4	4	4	4	4	4	4	4
End-members										
j (o)	0.48	0.47	0.49	0.50	0.49	0.48	0.51	0.49	0.48	0.48
f (o)	0.20	0.17	0.24	0.25	0.25	0.18	0.23	0.16	0.16	0.19
x (o)	0.08	0.12	0.03	0.00	0.01	0.10	0.02	0.13	0.13	0.10
p(jad)	0.39	0.39	0.37	0.37	0.37	0.39	0.39	0.41	0.40	0.39
p(diop)	0.48	0.47	0.50	0.50	0.50	0.47	0.48	0.45	0.45	0.47
p(hed)	0.04	0.07	0.01	0.00	0.00	0.05	0.01	0.06	0.07	0.05
p(aeg)	0.09	0.08	0.12	0.12	0.12	0.09	0.12	0.08	0.08	0.09

Analysis was performed on omphacite grains shown in Fig. 9a. j, f and x are the compositional variables of omphacite (as defined in the *a-x* model in THERMOCALC). j(o)= Na; f(o)= Fe^{3+} cations; and x(o)= $Fe^{2+}/(Fe^{2+}+Mg)$ ratio.

4.3. Pressure-Temperature conditions

P–T pseudosections were calculated for three rocks to provide a robust metamorphic framework for the deformation stages. The rocks chosen for calculations were based on the main deformation stages: pseudotachylite, HOL2A_2015 (Fig. 11); first completely eclogitised rock, HOL7C_2014 (Fig. 13a); and the retrogressive mica-rich eclogite, HOL13A_2015 (Fig. 14a).

4.3.1. HOL2A_2015 (RECRYSTALLISED PSEUDOTACHYLITE)

The result for phase equilibria modelling for the recrystallised pseudotachylite is shown in Figure 11. At this stage the model is incomplete due to the complexities involving different solvi in a very small part of *P–T* space. The peak assemblage, garnet–kyanite–plagioclase–K-feldspar–omphacite–zoisite/clinozoisite, was not successfully calculated. However, the pseudosection indicates that K-feldspar bearing assemblages recrystallised at pressures lower than 13.8 kbar.

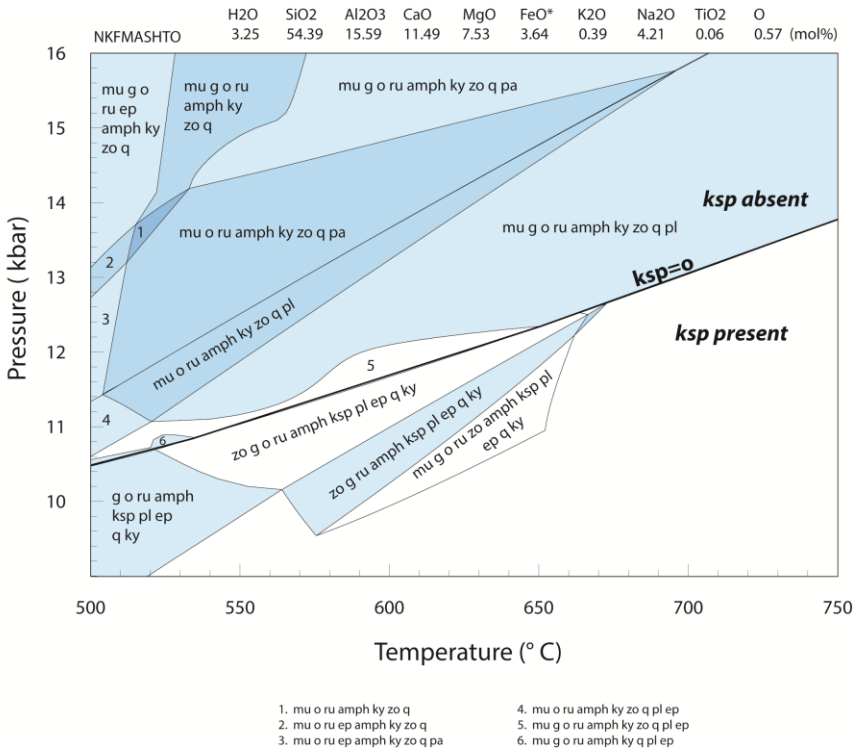

Figure 11. Incomplete calculated *P–T* pseudosection for HOL2A_2015. Labelled white fields have a variance of 2 while the darkest blue has a variance of 4. Mineral abbreviations used from Holland and Powell (1998).
The bold line is the K-feldspar = 0 line abundance line.

4.3.2. HOL7C_2014 (COMPLETE ECLOGITISATION)

Figure 12 was calculated to demonstrate how attempts to obtain robust *P–T* estimates of the Bergen arc eclogites are affected by the presence of relict granulitic garnet. *P–T* conditions were estimated, successfully, using this model (Fig. 11) as the identified peak mineral assemblage, phengite–garnet–rutile–kyanite–zoisite. However, the presence of the relict garnets from the granulite made the chemical composition of the system biased; there was too much garnet for the composition of the eclogite HOL7C_2014. For a more realistic model, the relict granulitic garnet was substracted from the composition and modelled (Fig. 13a)

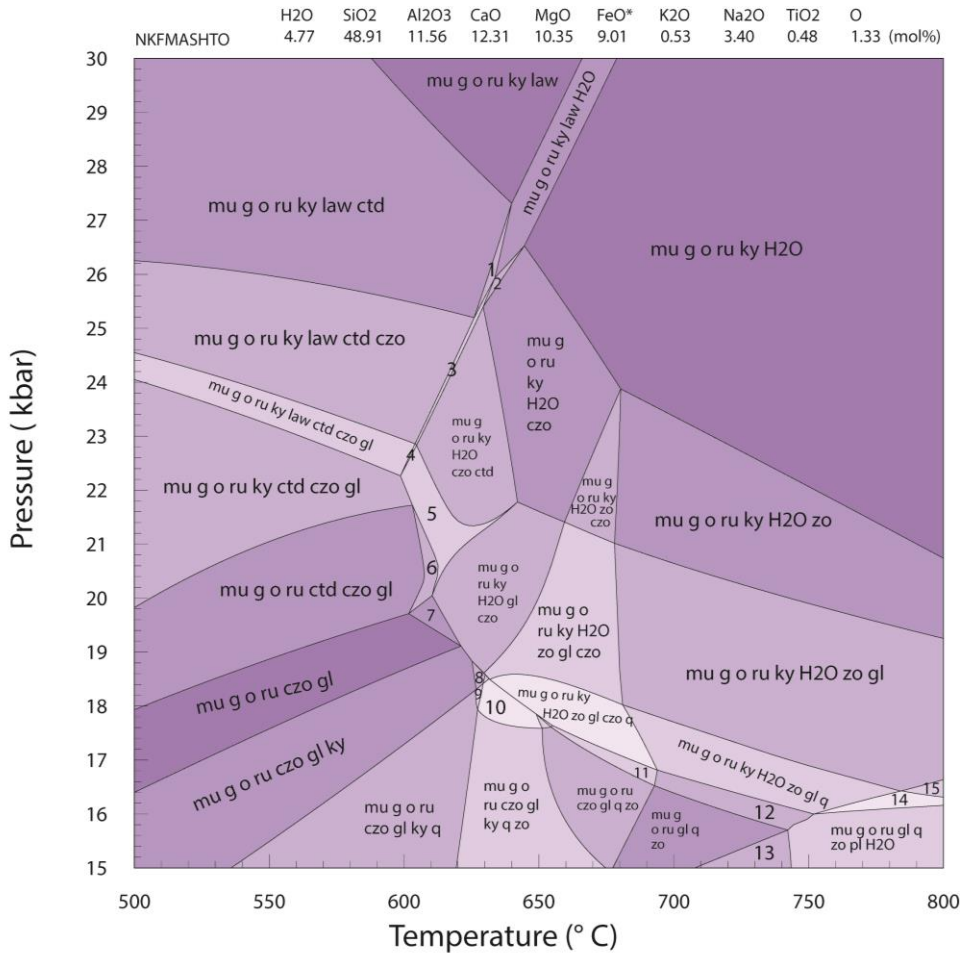

Figure 12. Calculated *P–T* pseudosection for unmodified bulk composition, HOL7C*, that contains 75.8% granulitic garnet. The bulk composition above the model is expressed as mol %). The paler coloured fields have a variance of two whereas the darkest shaded fields have variance of 6. Mineral abbreviations used from Holland and Powell (1998).
*tiny fields were not labelled.

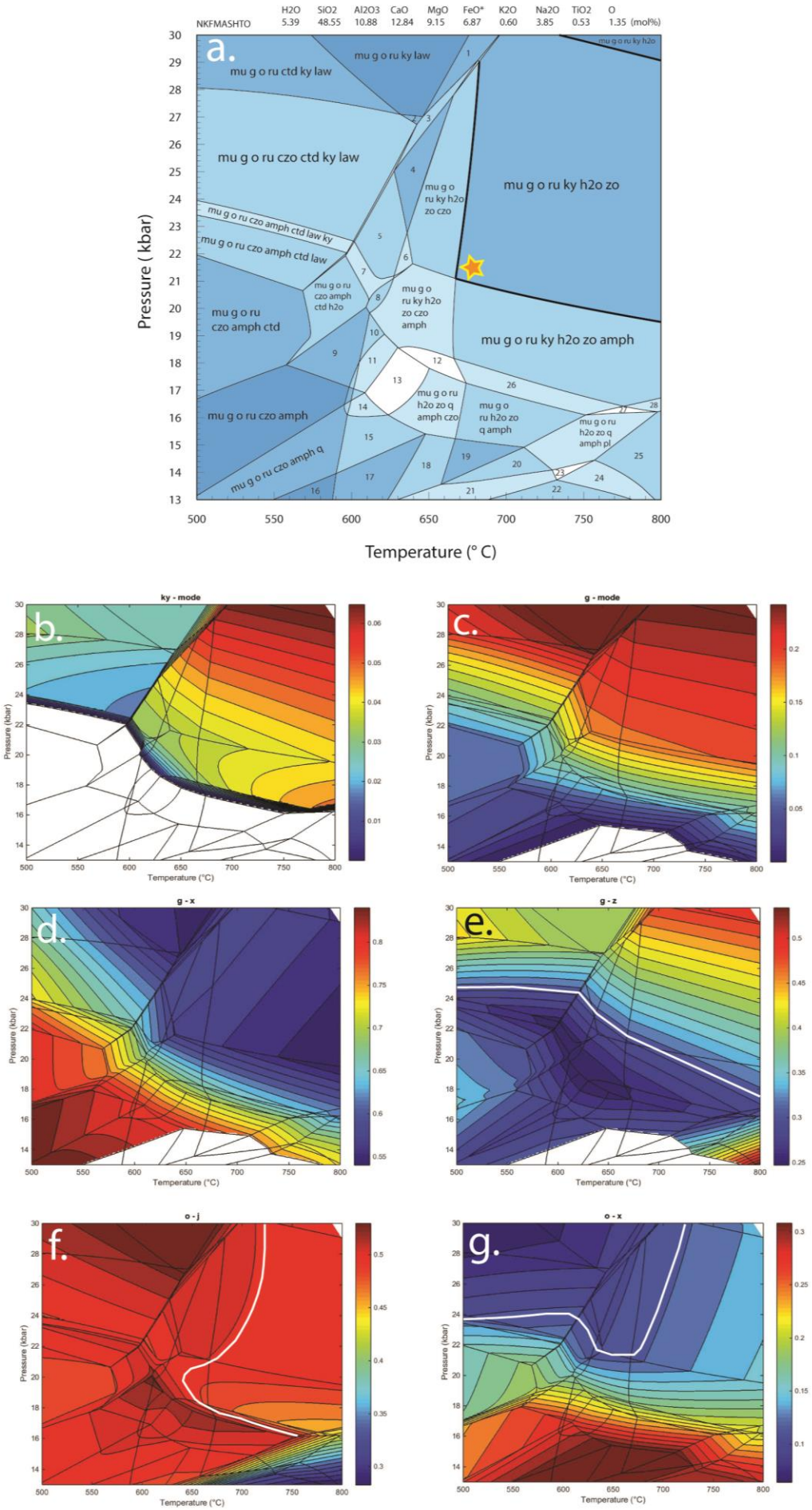

Figure 13. (a) Calculated *P–T* pseudosection for modified bulk composition (relict granulitic garnet removed) of sample HOL7C_2014. The bulk composition at top of model is expressed as mol %. The white fields have a variance of two whereas the darkest shade of blue indicates variance of six. Mineral abbreviations used from Holland and Powell (1998).
* tiny fields were not labelled and for full numerical label description, see Appendix A. Bold outline indicate peak mineral assemblage and orange star designates approximate *P–T* conditions.
(b-g) Contours were modelled as relative proportions ('modes') of the particular mineral in each field. Red represents higher percentages and blue the lowest. (b) Kyanite abundance contours. (c) Garnet abundance contours. (d) Garnet compositional contours for $x(g) = Fe^{2+}/(Fe^{2+} + Mg)$ cations. (e) Garnet compositional contours for $z(g) = Ca/(Fe^{2+} + Mg + Ca)$ cations. The maximum measured value was 0.29, plotted in white. (e) Omphacite compositional contours for $j(o)$= Na cations. The measured range was 0.48–0.50, plotted in white. (f) Omphacite compositional contours for $x(o) = Fe^{2+}/(Fe^{2+}+Mg)$ cations. The measured range was 0.10–0.13, plotted in white.

Figure 13 was calculated using the modified (i.e. granulitic garnet removed) composition for HOL7C_2014. The peak eclogite-facies assemblage phengite–garnet–omphacite–rutile–zoisite–kyanite–water, lies in the *P–T* range 21 to >30 kbar and 665 to >800 °C. This is a very large stability range for the assemblage. However, the peak *P–T* conditions can be tightly constrained within this large field using the TCInvestigator-generated plots of phase/mineral abundance and composition, Figures 13b–g. The measured Ca content of eclogitic garnet in the sample (z(g) = $X_{grossular}$ = Ca/(Ca + Fe + Mg) cations) is 0.29. The calculated compositional contour corresponding to z(g) = 0.29 is shown by the white line in Figure 13e. This white contour passes through the lower left-hand corner of the peak assemblage stability field. In addition, the abundance of kyanite in the sample is sufficiently low that kyanite was not captured in the elemental maps, Figure 9. Although x(g) (= Fe^{2+}/(Fe^{2+} + Mg) cations) varies little across the stability field of the peak assemblage, the values in the lower left corner of the field match well with the measured values (x(g) ~0.58–0.62 from Table 3). The measured compositions of omphacite (Table 5) are j(o) = Na cations ~0.48–0.50 and x(o) = Fe^{2+}/(Fe^{2+} + Mg) cations ~0.10–0.13 and plotted as white lines on Figure 13f and g. Although these compositions cover a large portion of the *P–T* model (especially j(o)) (Fig. 12f and g), they do correlate with the peak assemblage field. Combining all these together, the peak *P–T* conditions are constrained to about 21–22 kbar and 660–680 °C.

4.3.3. HOL13A_2015 (MICA-RICH ECLOGITE)

Figure 14a is the calculated *P–T* pseudosection for the last, retrogressive stage (Stage 5) of deformation and metamorphism.

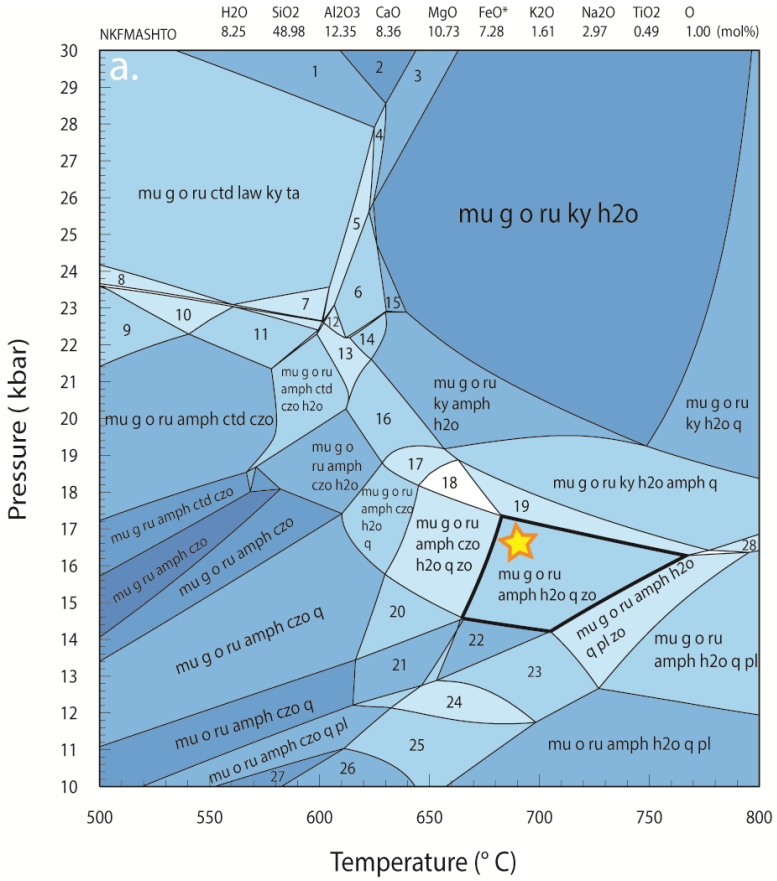

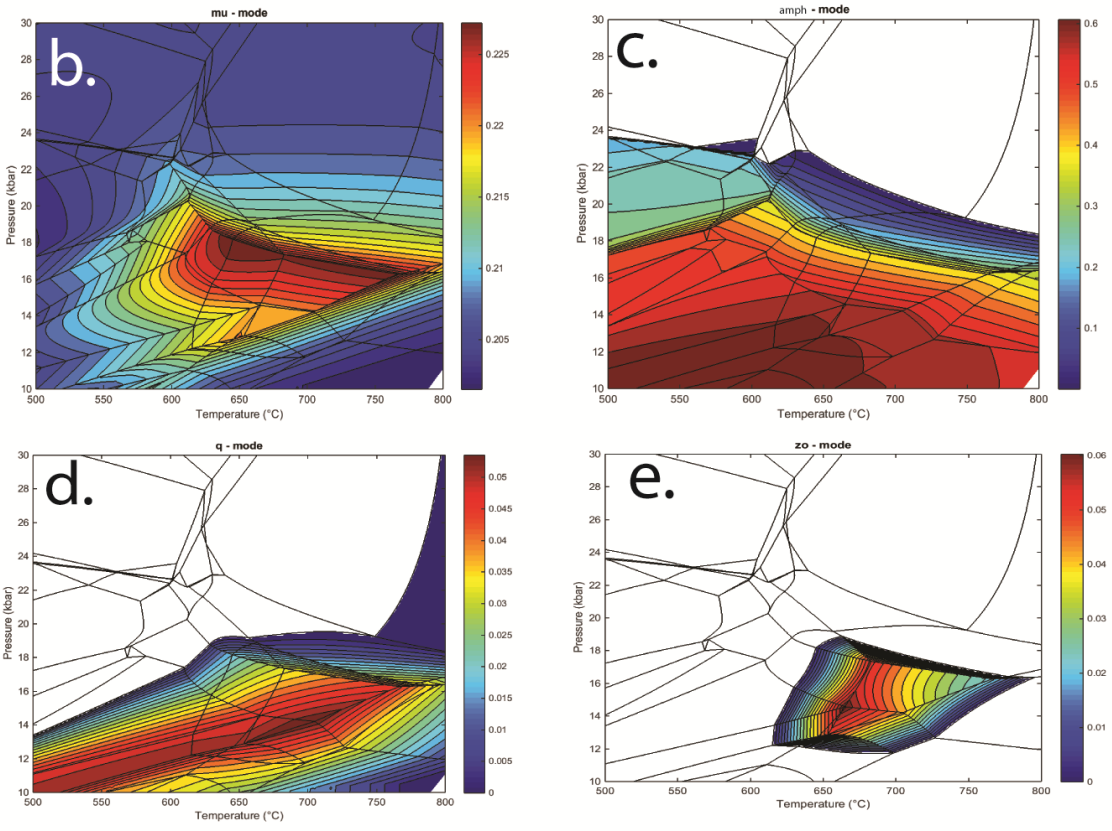

Figure 14. (a) Calculated *P–T* pseudosection for retrogressed eclogite, HOL13A_2015. The bulk composition at top of model is expressed as mol % . The white fields have a variance of two while the fields with darkest shade of blue have variance of seven. Mineral abbreviations used from Holland and Powell (1998). Bold outline indicates peak mineral assemblage and bright yellow star designates approximate inferred *P–T* conditions.*tiny fields were not labelled and for full numerical label description, see Appendix A (b–e) Contours were modelled as relative proportion ('modes') of the particular mineral in each field. Red represents higher percentages and blue the lowest. (b) Muscovite abundance contours. (c) amphibole abundance contours. (d) quartz abundance contours. (e) zoisite abundance contours.

The peak assemblage for HOL13A_2015, phengite–garnet–omphacite–rutile–amphibole–zoisite–quartz–water, lies in the *P–T* range 14.0–17.5 kbar and 650–760 °C. To further constrain the peak conditions, the modal proportions of phengite (Fig. 14b), amphibole (Fig. 14c), quartz (Fig. 14d) and zoisite (Fig. 14e) were taken into account within the peak assemblage. The resulting *P–T* conditions lay in range of 16–17 kbar and 680–700 °C.

5. DISCUSSION

The aim of this study is to provide the most robust *P–T* history (*i.e*: burial and exhumation constrains) yet for the eclogites on Holsnøy as setting up this framework has implications for better understanding the timing and potential source of the fluids causing the conversion of granulites to eclogites. Importantly, the *P–T* conditions are linked to the different stages of deformation that were identified through careful field observations and field geological mapping. Deformation and fluids have both played important roles in assisting the eclogitisation process at Holsnøy.

5.1. Pressure–Temperature evolution

Phase equilibria forward modelling has provided the basis for erecting a framework for the prograde, peak and retrograde *P–T* conditions of the eclogitisation process, *i.e*. define the *P–T* path of the process. The inferred *P–T* conditions for the pseudotachylite, eclogite and retrogressed eclogite are summarised on Figure 15.

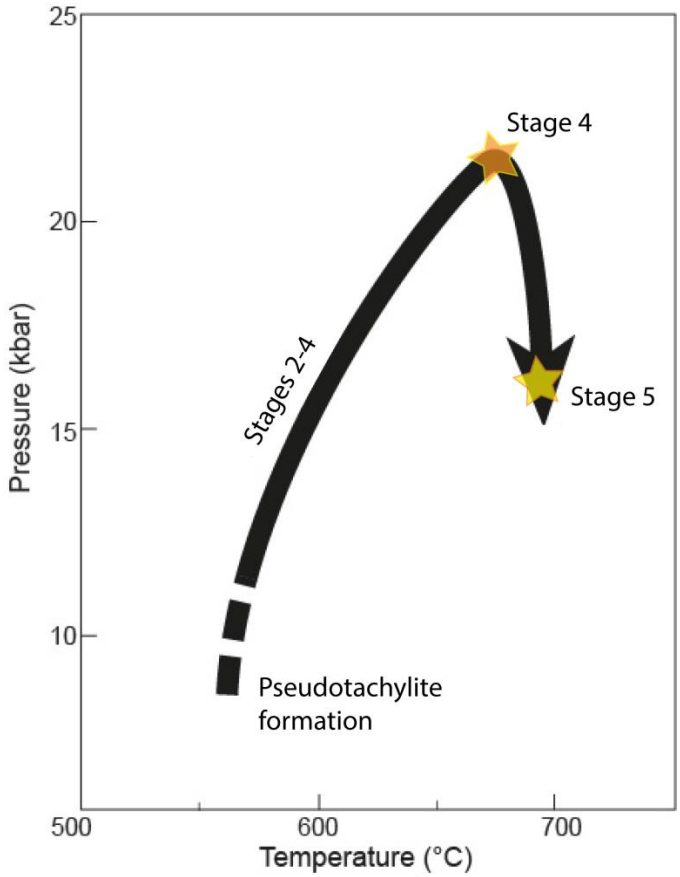

Figure 15. *P–T* path undergone by Holsnøy domains. Diagram was drawn based on the different models: Figure 11; Figure 13a (orange star representing inferred peak metamorphic field); Figure 14a (yellow star representing inferred peak metamorphic field).

The oldest structures that overprint the Mesoproterozoic granulites are the pseduotachylites which have recrystallised to fine-grained assemblages (Section 4.1). Even though the model is incomplete, it still provides good constraints on the *P–T* conditions at which the pseudotachylite recrystallised. The inferred peak mineral assemblage of HOL2A_2015 is garnet–kyanite–omphacite–zoisite/clinozoisite–plagioclase–K-feldspar–quartz–rutile with minor calcite and scapolite which were both not considered in the model. This assemblage cannot be defined on Figure 11. However, the incomplete model unambiguously defines the upper pressure limit of K-feldspar bearing assemblages in the recrystallised Stage 1 pseudotachylite to be between 10.5 and 13.8kbar for the range of temperatures realistically applicable to the Holsnøy rock system. This provides an upper

limit of ~ 35 km on the depths at which the pseudotachylite formed, and indicates that they formed within crust that had not undergone deep burial. This contrasts with a number previous works (*e.g.* Austrheim & Boundy 1994, Lund *et al.* 2004), who have used the presence of pseudotachylite within the Bergan Arc eclogites to argue for the existence of very deep seated (> 60 km) earthquakes.

Peak metamorphic conditions of the eclogite (HOL7C_2014) are constrained to be 21–22 kbar and 640–660 °C. These new estimates are in general agreement with the higher-*P* and lower-*T* estimates made from conventional thermobarometry (18–21 kbar and 650–800 °C) (Austrheim & Griffin 1985, Jamtveit *et al.* 1990, Pollok *et al.* 2008, Austrheim 2013). Nevertheless, there are numerous pitfalls associated with using conventional thermobarometry (Powell and Holland (2008). These include (possible) re-equilibration of mineral compositions with cooling, issues relating to accounting for Fe^{3+} in minerals (e.g. clinopyroxene), only using a small subset of the total mineral assemblage for thermobarometry, not knowing whether the derived *P–T* conditions actually occur inside the stability field of the assemblage, and the circular need to estimate *P* in order to calculate *T* and vice versa (Fitzsimons & Harley 1994, Pattison & Bégin 1994, Kelsey *et al.* 2003, Krogh Ravna & Terry 2004, Proyer *et al.* 2004, Powell & Holland 2008). Therefore, the use of pseudosections is a much more powerful approach to thermobarometry. Maximum pressures of 21–22 kbar equate to a maximum burial depth of about 70 km during the eclogitisation process.

P–T pseudosection and contours for the retrogressed, mica-rich eclogite (HOL13A_2015; Fig. 14) estimate Stage 5 deformation to have happened at 16–17 kbar and 680–700 °C. These lower *P–T* conditions, as well as the more hydrous mineralogy and field outcrop relationships, establish that that Stage 5 of deformation occurred on the retrograde path. The calculated conditions are close to the estimates of peak *P–T* conditions from earlier

studies (Austrheim & Griffin 1985). The data suggest that as the eclogites were being exhumed the rocks had access to additional fluid – possibly the same fluid responsible for creating eclogites at 21–22 kbar but present in greater abundance.

Due to the samples being specifically characterised within the framework of the stages of deformation and fluid evolution, it is possible to interpret that the *P–T* conditions recorded by each of the three samples are linked, in sequence, by a *P–T* evolution path. The interpreted *P–T* path for the Holsnøy eclogites is shown in Figure 15 and defines a clockwise evolution. If the retrograde path continued along a trajectory of decreasing pressure but with gradually increasing cooling, the rocks would end up in the amphibolite facies (which spans ~450–700 °C). Amphibolite facies reworking of the eclogites is documented elsewhere in the Bergen arcs (Andersen *et al.* 1991b, a, Boundy *et al.* 1992, Engvik *et al.* 2000, Bingen *et al.* 2001, Raimbourg *et al.* 2005, Glodny *et al.* 2008)

5.2. *P–T* constraints and fluid infiltration

In terms of fluid infiltration, Stage 2 of deformation (prior to peak eclogite) is known to undergo a significant reduction in the abundance of garnet (Fig. 4c) and some garnets have even been completely consumed by this stage of the eclogitisation process. Time constraints in the project precluded modelling of this particular stage of deformation. However, some general comments can be made from the mineralogical relationships associated with Stage 2 fluid–rock interaction. Even though the bulk compositions of fluid-affected rocks of Stage 2 and Stage 4 (peak eclogite stage; sample HOL7C_2014, Fig. 13c) are different, the difference is not significant (Table 1). This means that the general mineralogical relationships and associated trends in garnet modal proportions (relative abundance) shown in Figure 13c could act as a general guide to help us understand Stage 2. For example, in most metamorphic systems, the modal proportion of garnet is strongly positively correlated with pressure (Tracy

& Robinson 1976, Spear *et al.* 1984, Caddick *et al.* 2010) as shown in Figure 13c. Combining Figure 13c as a rough basis and the fact that the transition of the granulite to eclogite was enhanced by the presence of fluid (Andersen *et al.* 1991c, Austrheim 2013), for the garnet abundance to be so significantly reduced during Stage 2, fluid–rock interaction must have occurred at pressures well below the inferred peak pressures of ~22 kbar derived from Stage 4 of the fluid–rock system.

If this reasoning is applicable, then it implies that fluid infiltration occurred on the prograde path (burial). It is quite difficult to unambiguously demonstrate that fluid infiltration occurred during the more advanced stages of the eclogitisation process (Stage 3 and Stage 4). However, in each of these stages the relict granulite blocks have gradational margins with the enclosing eclogite. This suggests that Stages 3 and 4 were associated with the ongoing conversion of granite to eclogite.

During Stage 5, localised domains of coarse-grained phengite–garnet–clinopyroxene–amphibole–zoisite–rutile–quartz overprint less muscovite-rich eclogite (Fig. 7). *P–T* modelling of these mica-rich rocks indicates pressures around 16 kbar (Fig. 14), well below the peak pressures. This implies a continued fluid-driven recrystallisation on the retrograde path.

5.3. Tectonic significance of fluid infiltration.

The process of exhumation is poorly understood. However, there are some important points to emphasise on regarding fluid–rock interactions. Firstly, the eclogites are generally denser than the granulite (Austrheim 1987, Lardeaux & Spalla 1991, Massonne *et al.* 2007) which implies that exhumation should be thwarted. However, Jolivet *et al.* (2005) argue that most of the eclogites on Holsnøy are only partially eclogitised, hence overall the transformed rock will have a bulk density between that of the granulite and eclogites. It may be that an

unknown quantity of more-completely eclogitised rock was subducted into the mantle and was unable to be exhumed due to negative buoyancy.

Secondly, previous studies have shown that the strength of the rocks is significantly reduced by the eclogitisation process. It is quite noticeable that shear deformation only occurs in the eclogitised domain (Stages 3 onwards) (Lardeaux & Spalla 1991, Boundy *et al.* 1992, Engvik *et al.* 2000, Austrheim 2013). To provide a possible explanation for the exhumation of the Bergen Arcs, Jolivet *et al.* (2005) proposed the following model (Fig. 16).

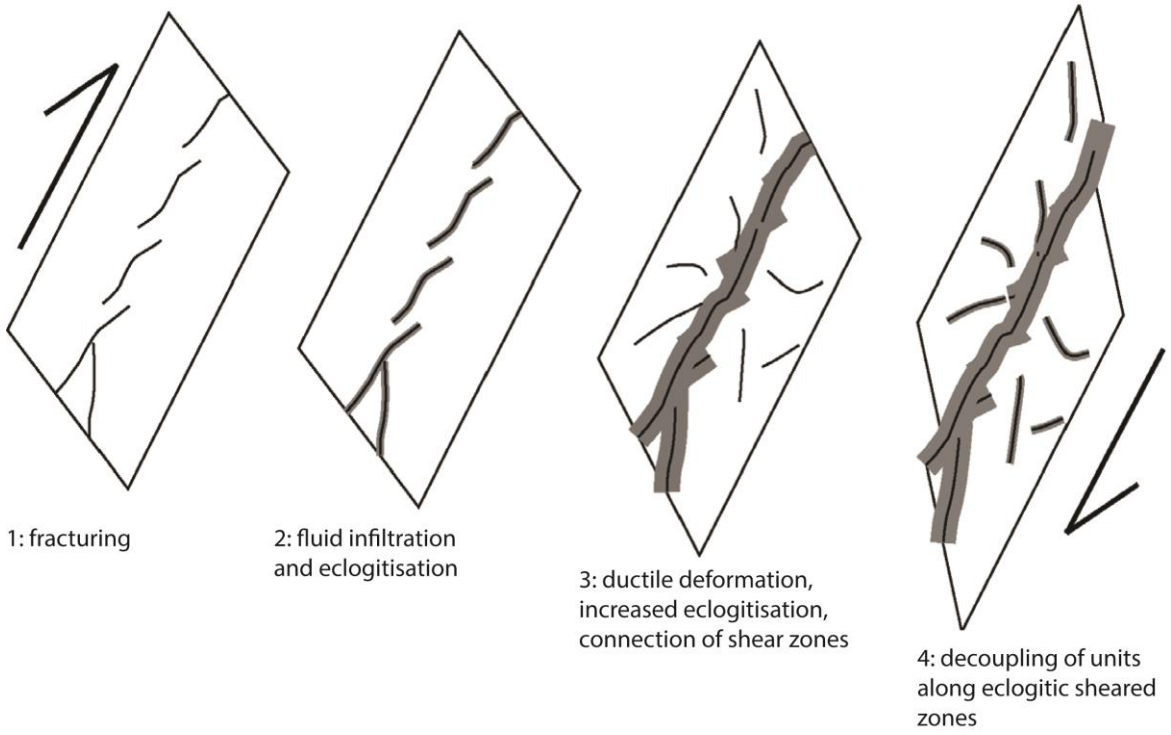

Figure 16. Model adapted from Jolivet *et al.* (2005) showing the progressive shearing of domains as fluid infiltrated.

The last stage of the Jolivet *et al*. model which allows for the exhumation of the unit is the decoupling of rock masses along shear zones (Fig. 6d and Fig. 16). Since the granulite is only partially eclogitised, the granulite + eclogite rock masses are still buoyant enough to detach themselves from other parts of the subducting rock mass and exhume along the subduction channel. In this model, the role of fluid is of great significance as it is the element

that potentially weakens the domains. This is analogous to the presence of partial melt which is invoked as a critical rheological agent in facilitating exhumation of ultrahigh-pressure (diamond and/or coesite-bearing) rocks along subduction (Hermann *et al.* 2001, Labrousse *et al.* 2011, Labrousse *et al.* 2015).

6. CONCLUSIONS

Detailed geological mapping on the island of Holsnøy in the Bergen Arcs, Norway, documents a progression from localised brittle structures and pseudotachylite to increasingly voluminous fluid involved deformation culminating in the large-scale conversion of anorthositic granulite to eclogite. Phase equilibria forward modelling from (1) prograde mineral assemblages preserved in areas of limited fluid-rock interaction, (2) assemblages developed within voluminous peak eclogite and (3) assemblages developed in retrograde fluid-rich domains, document a burial and partial exhumation path. Moreover, the *P–T* models show that the anorthositic granulite on Holsnøy experienced long-lived (prograde, peak and retrograde) fluid infiltration driven recrystallisation during the subduction of anorthositic crust. This study provides a sound platform for further work to address the absolute timing, source and composition of the fluids.

7. ACKNOWLEDGMENTS

Supervisors Martin Hand and David Kelsey are thanked for their continued support and help throughout the project. Thank you to Chris Clark, Curtin University, for generously funding the study and Luke Hersey, Curtin University, for his help with the mapping part of the project. Naomi Tucker and Laura Morrissey are also thanked for their invaluable guidance with THERMOCALC. Ben Wade, Angus Netting and Aoife McFadden, Adelaide Microscopy, are thanked for their assistance with the electron microprobe. Lastly, Mark Pearce, CSIRO, is thanked for his incredible help with TCInvestigator.

8. REFERENCES

ANDERSEN T., AUSTRHEIM H. & BURKE E. 1990. Fluid inclusions in granulites and eclogites from the Bergen Arcs, Caledonides of W. Norway. *Mineralogical Magazine* **54**, 145-158.

ANDERSEN T., AUSTRHEIM H. & BURKE E. 1991a. Fluid-induced retrogression of granulites in the Bergen Arcs, Caledonides of W. Norway: Fluid inclusion evidence from amphibolite-facies shear zones. *Lithos* **27**, 29-42.

ANDERSEN T., AUSTRHEIM H. & BURKE E. 1991b. Mineral-fluid-melt interactions in high-pressure shear zones in the Bergen Arcs nappe complex, Caledonides of W. Norway: Implications for the fluid regime in Caledonian eclogite-facies metamorphism. *Lithos* **27**, 187-204.

ANDERSEN T., AUSTRHEIM H., BURKE E. A. & ELVEVOLD S. 1993. N 2 and CO 2 in deep crustal fluids: evidence from the Caledonides of Norway. *Chemical Geology* **108**, 113-132.

ANDERSEN T., AUSTRHEIM H. & BURKE E. A. J. 1991c. Mineral-fluid-melt interactions in high-pressure shear zones in the Bergen Arcs nappe complex, Caledonides of W. Norway: Implications for the fluid regime in Caledonian eclogite-facies metamorphism. *Lithos* **27**, 187-204.

AUSTRHEIM H. 1987. Eclogitization of lower crustal granulites by fluid migration through shear zones. *Earth and Planetary Science Letters* **81**, 221-232.

AUSTRHEIM H. 2013. Fluid and deformation induced metamorphic processes around Moho beneath continent collision zones: Examples from the exposed root zone of the Caledonian mountain belt, W-Norway. *Tectonophysics* **609**, 620-635.

AUSTRHEIM H. & BOUNDY T. 1994. Pseudotachylytes generated during seismic faulting and eclogitization of the deep crust. *Science* **265**, 82-83.

AUSTRHEIM H., ERAMBERT M. & ENGVIK A. K. 1997. Processing of crust in the root of the Caledonian continental collision zone: the role of eclogitization. *Tectonophysics* **273**, 129-153.

AUSTRHEIM H. & GRIFFIN W. L. 1985. Shear deformation and eclogite formation within granulite-facies anorthosites of the Bergen Arcs, western Norway. *Chemical Geology* **50**, 267-281.

BINGEN B., AUSTRHEIM H., WHITEHOUSE M. J. & DAVIS W. J. 2004. Trace element signature and U–Pb geochronology of eclogite-facies zircon, Bergen Arcs, Caledonides of W Norway. *Contributions to mineralogy and petrology* **147**, 671-683.

BINGEN B., DAVIS W. J. & AUSTRHEIM H. 2001. Zircon U-Pb geochronology in the Bergen arc eclogites and their Proterozoic protoliths, and implications for the pre-Scandian evolution of the Caledonides in western Norway. *Geological Society of America Bulletin* **113**, 640-649.

BOUNDY T., FOUNTAIN D. & AUSTRHEIM H. 1992. Structural development and petrofabrics of eclogite facies shear zones, Bergen Arcs, western Norway: implications for deep crustal deformational processes. *Journal of metamorphic geology* **10**, 127-146.

BOUNDY T. M., ESSENE E. J., HALL C. M., AUSTRHEIM H. & HALLIDAY A. 1996. Rapid exhumation of lower crust during continent-continent collision and late extension: Evidence from 40Ar/39Ar incremental heating of hornblendes and muscovites, Caledonian orogen, western Norway. *Geological Society of America Bulletin* **108**, 1425-1437.

BOUNDY T. M., MEZGER K. & ESSENE E. J. 1997. Temporal and tectonic evolution of the granulite-eclogite association from the Bergen Arcs, western Norway. *Lithos* **39**, 159-178.

CADDICK M. J., KONOPÁSEK J. & THOMPSON A. B. 2010. Preservation of garnet growth zoning and the duration of prograde metamorphism. *Journal of petrology* **51**, 2327-2347.

CARSWELL D., BRUECKNER H., CUTHBERT S., MEHTA K. & O'BRIEN P. 2003. The timing of stabilisation and the exhumation rate for ultra-high pressure rocks in the Western Gneiss Region of Norway. *Journal of metamorphic geology* **21**, 601-612.

CENTRELLA S., AUSTRHEIM H. & PUTNIS A. 2015. Coupled mass transfer through a fluid phase and volume preservation during the hydration of granulite: An example from the Bergen Arcs, Norway. *Lithos*.

COGGON R. & HOLLAND T. 2002. Mixing properties of phengitic micas and revised garnet-phengite thermobarometers. *Journal of metamorphic geology* **20**, 683-696.

CONNOLLY J. 2005. Computation of phase equilibria by linear programming: a tool for geodynamic modeling and its application to subduction zone decarbonation. *Earth and Planetary Science Letters* **236**, 524-541.

CONNOLLY J. 2009. The geodynamic equation of state: what and how. *Geochemistry, Geophysics, Geosystems* **10**.

CONNOLLY J. & PETRINI K. 2002. An automated strategy for calculation of phase diagram sections and retrieval of rock properties as a function of physical conditions. *Journal of metamorphic geology* **20**, 697-708.

DE PAOLI M., CLARKE G., KLEPEIS K., ALLIBONE A. & TURNBULL I. 2009. The eclogite–granulite transition: mafic and intermediate assemblages at Breaksea Sound, New Zealand. *Journal of petrology*, egp078.

DIENER J. & POWELL R. 2012. Revised activity–composition models for clinopyroxene and amphibole. *Journal of metamorphic geology* **30**, 131-142.

DIENER J., POWELL R., WHITE R. & HOLLAND T. 2007. A new thermodynamic model for clino- and orthoamphiboles in the system Na2O–CaO–FeO–MgO–Al2O3–SiO2–H2O–O. *Journal of metamorphic geology* **25**, 631-656.

EIDE E., TORSVIK T., ANDERSEN T. & ARNAUD N. 1999. Early Carboniferous unroofing in western Norway: A tale of alkali feldspar thermochronology. *The Journal of Geology* **107**, 353-374.

ENGVIK A. K., AUSTRHEIM H. & ANDERSEN T. B. 2000. Structural, mineralogical and petrophysical effects on deep crustal rocks of fluid-limited polymetamorphism, Western Gneiss Region, Norway. *Journal of the Geological Society* **157**, 121-134.

ERAMBERT M. & AUSTRHEIM H. 1993. The effect of fluid and deformation on zoning and inclusion patterns in poly-metamorphic garnets. *Contributions to mineralogy and petrology* **115**, 204-214.

FITZSIMONS I. & HARLEY S. 1994. The influence of retrograde cation exchange on granulite PT estimates and a convergence technique for the recovery of peak metamorphic conditions. *Journal of petrology* **35**, 543-576.

FROST B. R. & CHACKO T. 1989. The granulite uncertainty principle: limitations on thermobarometry in granulites. *The Journal of Geology*, 435-450.

GLODNY J., KÜHN A. & AUSTRHEIM H. 2008. Geochronology of fluid-induced eclogite and amphibolite facies metamorphic reactions in a subduction–collision system, Bergen Arcs, Norway. *Contributions to mineralogy and petrology* **156**, 27-48.

GREEN E., HOLLAND T. & POWELL R. 2007. An order-disorder model for omphacitic pyroxenes in the system jadeite-diopsidehedenbergite-acmite, with applications to eclogitic rocks. *American Mineralogist* **92**, 1181-1189.

HACKER B. R., ANDERSEN T. B., JOHNSTON S., KYLANDER-CLARK A. R., PETERMAN E. M., WALSH E. O. & YOUNG D. 2010. High-temperature deformation during continental-margin

subduction & exhumation: The ultrahigh-pressure Western Gneiss Region of Norway. *Tectonophysics* **480**, 149-171.

HERMANN J., RUBATTO D., KORSAKOV A. & SHATSKY V. S. 2001. Multiple zircon growth during fast exhumation of diamondiferous, deeply subducted continental crust (Kokchetav Massif, Kazakhstan). *Contributions to mineralogy and petrology* **141**, 66-82.

HOLLAND T. & POWELL R. 1998. An internally consistent thermodynamic data set for phases of petrological interest. *Journal of metamorphic geology* **16**, 309-343.

HOLLAND T. & POWELL R. 2003. Activity–composition relations for phases in petrological calculations: an asymmetric multicomponent formulation. *Contributions to mineralogy and petrology* **145**, 492-501.

HOLLAND T. & POWELL R. 2011. An improved and extended internally consistent thermodynamic dataset for phases of petrological interest, involving a new equation of state for solids. *Journal of metamorphic geology* **29**, 333-383.

HORA J., SIMON K., KRONZ A., XIAO Y. & WORNER G. 2014. Comparison of Geothermobarometers with Different Closure Behavior to Constrain PT Paths. *AGU Fall Meeting Abstracts*, p. 4778.

JAMTVEIT B., BUCHER-NURMINEN K. & AUSTRHEIM H. 1990. Fluid controlled eclogitization of granulites in deep crustal shear zones, Bergen arcs, Western Norway. *Contributions to mineralogy and petrology* **104**, 184-193.

JOLIVET L., RAIMBOURG H., LABROUSSE L., AVIGAD D., LEROY Y., AUSTRHEIM H. & ANDERSEN T. B. 2005. Softening trigerred by eclogitization, the first step toward exhumation during continental subduction. *Earth and Planetary Science Letters* **237**, 532-547.

KELSEY D., WHITE R. & POWELL R. 2003. Orthopyroxene–sillimanite–quartz assemblages: distribution, petrology, quantitative P–T–X constraints and P–T paths. *Journal of metamorphic geology* **21**, 439-453.

KROGH E. J. 1977. Evidence of Precambrian continent-continent collision in Western Norway. *Nature* **267**, 17-19.

KROGH RAVNA E. & TERRY M. P. 2004. Geothermobarometry of UHP and HP eclogites and schists–an evaluation of equilibria among garnet–clinopyroxene–kyanite–phengite–coesite/quartz. *Journal of metamorphic geology* **22**, 579-592.

KÜHN A., GLODNY J., AUSTRHEIM H. & RAHEIM A. 2002. The Caledonian tectono-metamorphic evolution of the Lindas Nappe: constraints from U-Pb, Sm-Nd and Rb-Sr ages of granitoid dykes. *Norsk Geologisk Tidsskrift* **82**, 45-58.

LABROUSSE L., DURETZ T. & GERYA T. 2015. H 2 O-fluid-saturated melting of subducted continental crust facilitates exhumation of ultrahigh-pressure rocks in continental subduction zones. *Earth and Planetary Science Letters* **428**, 151-161.

LABROUSSE L., PROUTEAU G. & GANZHORN A.-C. 2011. Continental exhumation triggered by partial melting at ultrahigh pressure. *Geology* **39**, 1171-1174.

LARDEAUX J. & SPALLA M. 1991. From granulites to eclogites in the Sesia zone (Italian Western Alps): a record of the opening and closure of the Piedmont ocean. *Journal of metamorphic geology* **9**, 35-59.

LUND M. G., AUSTRHEIM H. & ERAMBERT M. 2004. Earthquakes in the deep continental crust-insights from studies on exhumed high-pressure rocks. *Geophysical Journal International* **158**, 569-576.

MARTIN L. A., RUBATTO D., BROVARONE A. V. & HERMANN J. 2011. Late Eocene lawsonite-eclogite facies metasomatism of a granulite sliver associated to ophiolites in Alpine Corsica. *Lithos* **125**, 620-640.

MASSONNE H.-J., WILLNER A. P. & GERYA T. 2007. Densities of metapelitic rocks at high to ultrahigh pressure conditions: What are the geodynamic consequences? *Earth and Planetary Science Letters* **256**, 12-27.

MATTEY D., JACKSON D., HARRIS N. & KELLEY S. 1994. Isotopic constraints on fluid infiltration from an eclogite facies shear zone, Holsenøy, Norway. *Journal of metamorphic geology* **12**, 311-325.

PATTISON D. & BÉGIN N. 1994. Zoning patterns in orthopyroxene and garnet in granulites: implications for geothermometry. *Journal of metamorphic geology* **12**, 387-410.

PATTISON D. R., CHACKO T., FARQUAR J. & MCFARLANE C. R. 2003. Temperatures of granulite-facies metamorphism: constraints from experimental phase equilibria and thermobarometry corrected for retrograde exchange. *Journal of petrology* **44**, 867-900.

PEARCE M., GAZLEY M. & WHITE A. 2014. TC-Investigator: A Matlab Program to Explore Pseudosections. *EGU General Assembly Conference Abstracts*, p. 14253.

PEARSON N. J., O'REILLY S. Y. & GRIFFIN W. L. 1991. The granulite to eclogite transition beneath the eastern margin of the Australian craton. *European Journal of Mineralogy*, 293-322.

POLLOK K., LLOYD G. E., AUSTRHEIM H. & PUTNIS A. 2008. Complex replacement patterns in garnets from Bergen Arcs eclogites: a combined EBSD and analytical TEM study. *Chemie der Erde-Geochemistry* **68**, 177-191.

POWELL R. & HOLLAND T. 2008. On thermobarometry. *Journal of metamorphic geology* **26**, 155-179.

PROYER A., DACHS E. & MCCAMMON C. 2004. Pitfalls in geothermobarometry of eclogites: Fe3+ and changes in the mineral chemistry of omphacite at ultrahigh pressures. *Contributions to mineralogy and petrology* **147**, 305-318.

RAIMBOURG H., JOLIVET L., LABROUSSE L., LEROY Y. & AVIGAD D. 2005. Kinematics of syn-eclogite deformation in the Bergen Arcs, Norway, implications for exhumation mechanisms. *Special Publication-Geological Society of London* **243**, 175-192.

ROCKOW K. M., HASKIN L. A. & FOUNTAIN D. 1997. Constraints on element mobility associated with the conversion of granulite to eclogite along fractures in an anorthositic complex on Holsnøy, Norway. *Journal of metamorphic geology* **15**, 401-418.

RUSSELL A. K., KITAJIMA K., STRICKLAND A., MEDARIS L. G., SCHULZE D. J. & VALLEY J. W. 2012. Eclogite-facies fluid infiltration: constraints from δ18O zoning in garnet. *Contributions to mineralogy and petrology* **165**, 103-116.

SCHULTE B. & SINDERN S. 2002. K-rich fluid metasomatism at high-pressure metamorphic conditions: Lawsonite decomposition in rodingitized ultramafite of the Maksyutovo Complex, Southern Urals (Russia). *Journal of metamorphic geology* **20**, 529-541.

SPEAR F. S., SELVERSTONE J., HICKMOTT D., CROWLEY P. & HODGES K. 1984. PT paths from garnet zoning: a new technique for deciphering tectonic processes in crystalline terranes. *Geology* **12**, 87-90.

TERRY M. & HEIDELBACH F. 2006. Deformation-enhanced metamorphic reactions and the rheology of high-pressure shear zones, Western Gneiss Region, Norway. *Journal of metamorphic geology* **24**, 3-18.

TRACY R. J. & ROBINSON P. 1976. Garnet composition and zoning in the determination of temperature and pressure of metamorphism, central Massachusetts.

TUCKER R., RÅHEIM A., KROGH T. & CORFU F. 1987. Uranium-lead zircon and titanite ages from the northern portion of the Western Gneiss Region, south-central Norway. *Earth and Planetary Science Letters* **81**, 203-211.

VAN WYCK N., VALLEY J. W. & AUSTRHEIM H. 1996. Oxygen and carbon isotopic constraints on the development of eclogites, Holsnøy, Norway. *Lithos* **38**, 129-145.

WHITE R., POWELL R. & HOLLAND T. 2007. Progress relating to calculation of partial melting equilibria for metapelites. *Journal of metamorphic geology* **25**, 511-527.

WHITE R., POWELL R., HOLLAND T. & WORLEY B. 2000. The effect of TiO~ 2 and Fe~ 2O~ 3 on metapelitic assemblages at greenschist and amphibolite facies conditions: mineral equilibria calculations in the system K~ 2O-FeO-MgO-Al~ 2O~ 3-SiO~ 2-H~ 2O-TiO~ 2-Fe~ 2O~ 3. *Journal of metamorphic geology* **18**, 497-512.

APPENDIX A: DETAILED PSEUDOSECTIONS

*HOL7C*_2014*

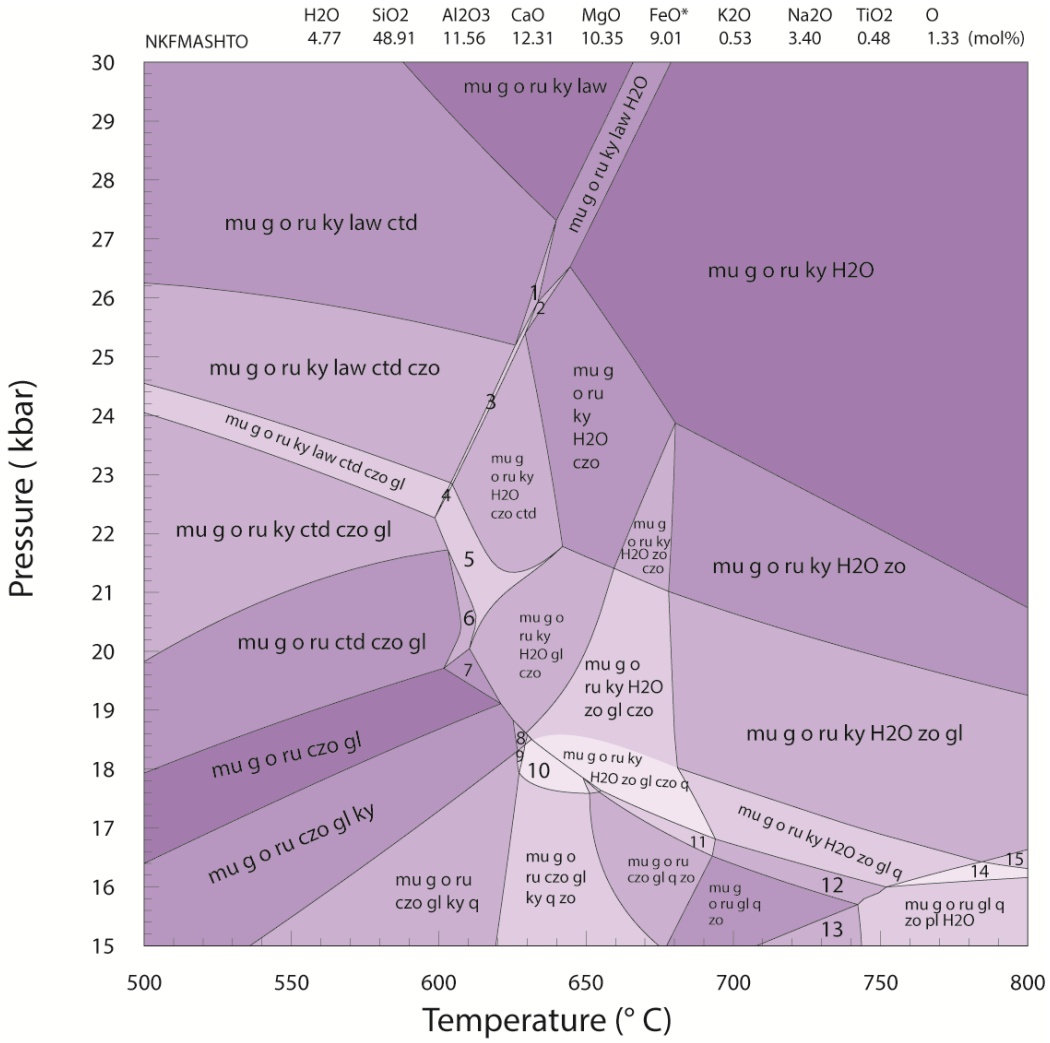

1. mu g o ru ky law ctd H2O
2. mu g o ru ky law H2O czo
3. mu g o ru ky law H2O czo ctd
4. mu g o ru ky law H2O czo ctd gl
5. mu g o ru ky H2O czo ctd gl
6. mu g o ru H2O czo ctd gl
7. mu g o ru H2O czo gl
8. mu g o ru czo gl ky H2O
9. mu g o ru czo gl ky H2O q
10. mu g o ru czo gl ky q zo pa
11. mu g o ru czo gl q zo H2O
12. mu g o ru gl q zo H2O
13. mu g o ru gl q zo pl
14. mu g o ru gl q zo pl H2O ky
15. mu g o ru gl zo pl H2O ky

HOL7C_2014 (MODIFIED BULK-COMPOSITION)

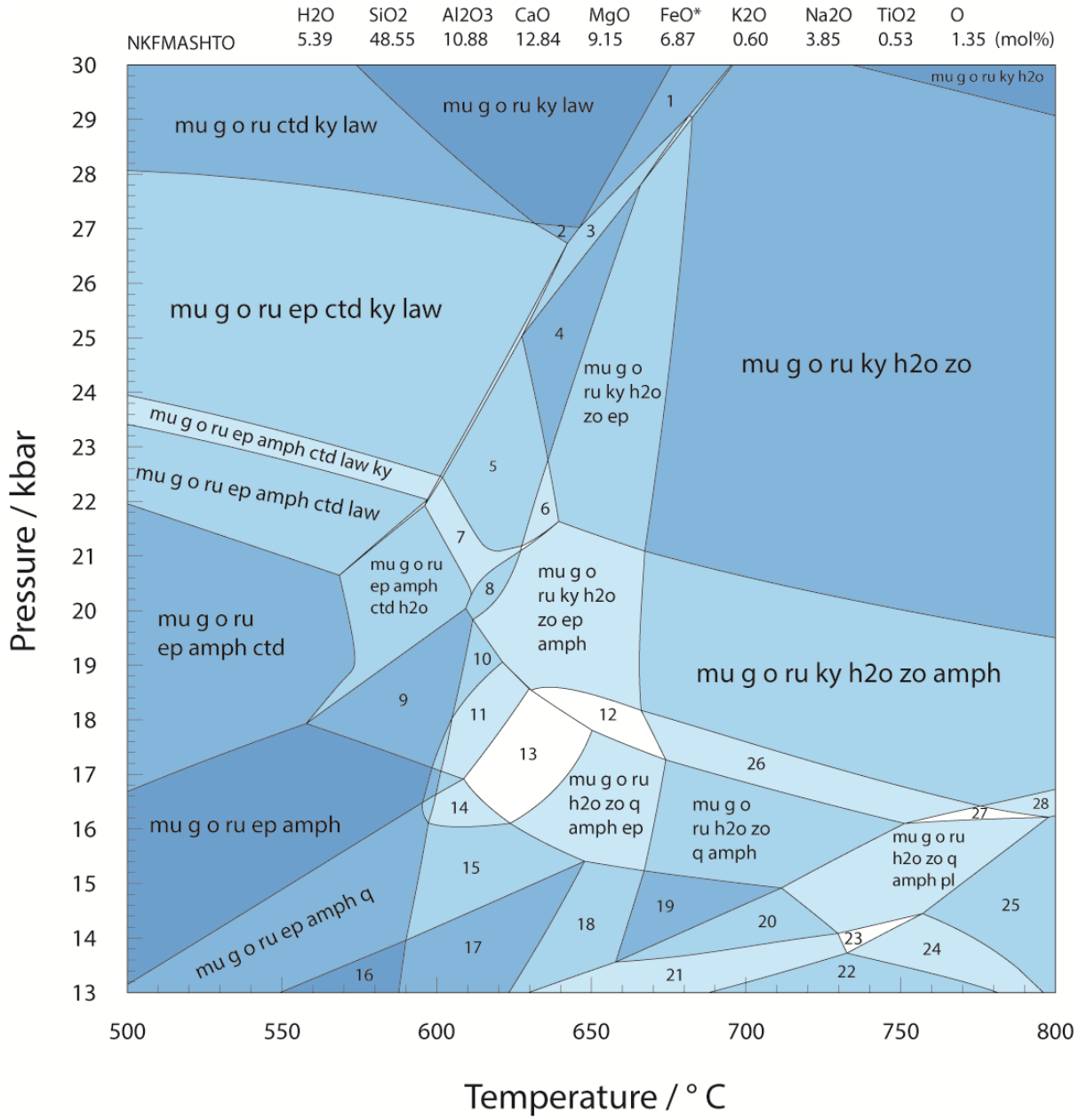

1. mu g o ru ky law h2o
2. mu g o ru ky law ep
3. mu g o ru ky law h2o ep
4. mu g o ru ky h2o ep
5. mu g o ru ky h2o ep ctd
6. mu g o ru ky h2o ep ctd zo
7. mu g o ru ky h2o ep ctd amph
8. mu g o ru ky h2o ep amph
9. mu g o ru h2o ep amph
10. mu g o ru h2o ep amph zo
11. mu g o ru h2o ep amph zo pa
12. mu g o ru ky h2o ep amph zo q
13. mu g o ru h2o ep amph zo pa q
14. mu g o ru ep amph zo pa q
15. mu g o ru ep amph zo q
16. mu o ru ep amph q
17. mu o ru ep amph zo q
18. mu o ru h2o ep amph zo q
19. mu o ru h2o amph zo q
20. mu o ru h2o amph zo q pl
21. mu o ru h2o ep amph zo q pl
22. mu o ru h2o ep amph zo pl
23. mu g o ru h2o ep amph zo pl q
24. mu g o ru h2o ep amph zo pl
25. mu g o ru h2o amph zo pl
26. mu g o ru ky h2o amph zo q
27. mu g o ru ky h2o amph zo q pl
28. mu g o ru ky h2o amph zo pl

HOL13A_2015

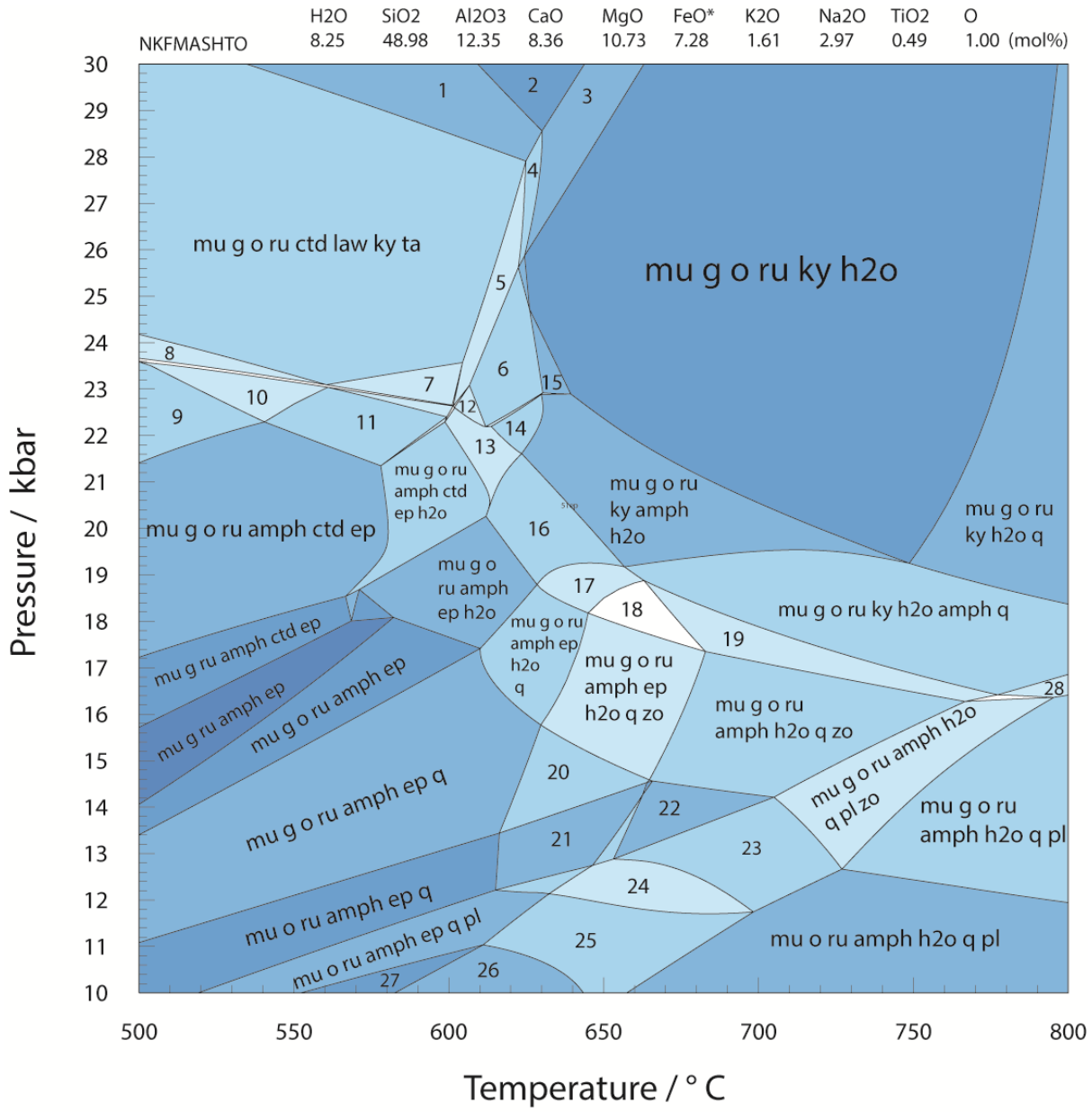

1. mu g o ru ctd law ky
2. mu g o ru law ky
3. mu g o ru law ky h2o
4. mu g o ru ctd law ky h2o
5. mu g o ru ctd law ky h2o ta
6. mu g o ru ctd ky h2o ta
7. mu g o ru gl ctd law ky ta
8. mu g o ru ctd law ky ta ep
9. mu g o ru amph ctd ep ta
10. mu g o ru amph ctd law ep ta
11. mu g o ru amph ctd law ep
12. mu g o ru ctd ep ky h2o ta
13. mu g o ru amph ctd ep ky h2o
14. mu g o ru amph ctd ky h2o
15. mu g o ru ky h2o ta
16. mu g o ru ep ky amph h2o
17. mu g o ru ep ky amph h2o q
18. mu g o ru ep ky amph h2o q zo
19. mu g o ru ky amph h2o q zo
20. mu g o ru amph ep q zo
21. mu o ru amph ep q zo
22. mu o ru amph h2o q zo
23. mu o ru amph h2o q zo pl
24. mu o ru amph ep h2o q zo pl
25. mu o ru amph ep h2o q pl
26. mu ru amph ep h2o q pl
27. mu ru amph ep q pl
28. mu g o ru amph ky h2o q pl

APPENDIX B: ADDITIONAL CONTOURS FOR HOL7C_2014 AND HOL13A_2015

HOL7C_2014

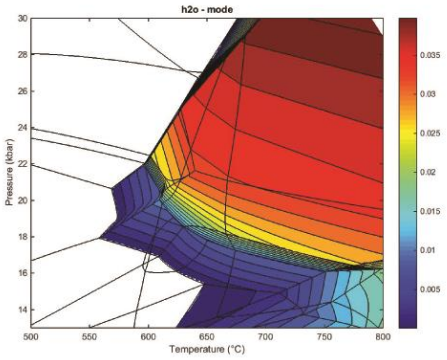

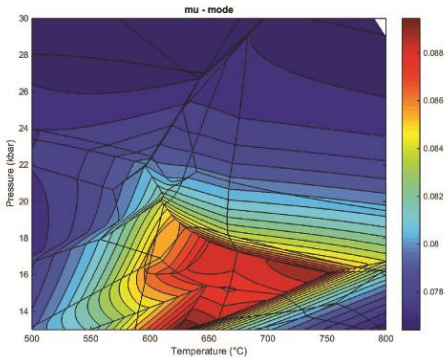

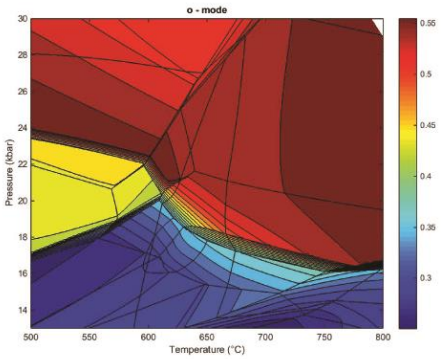

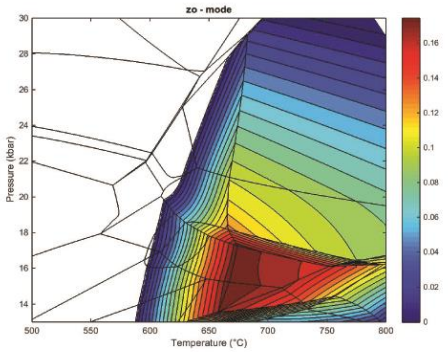

HOL13A

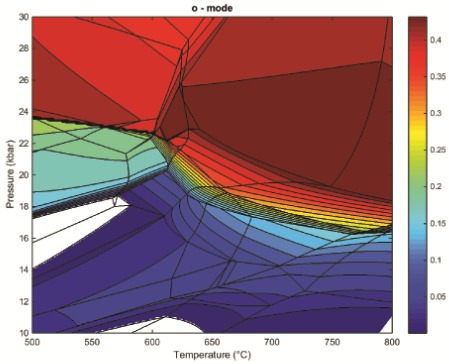

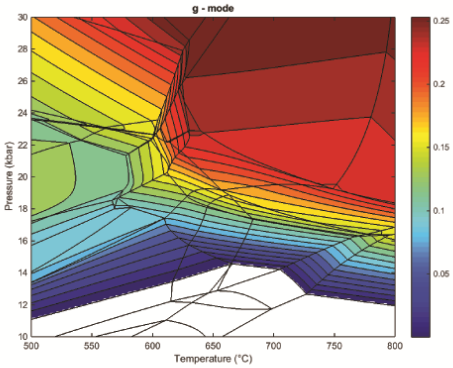

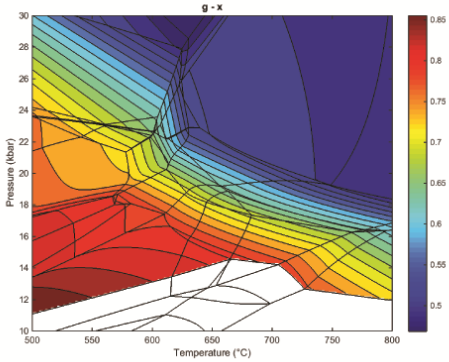

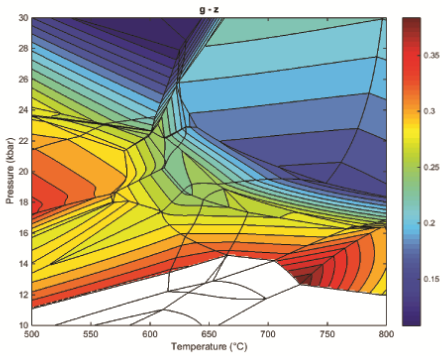

APPENDIX D: ADDITIONAL X-RAY MAPS

HOL7C_2014: GARNET MAPS

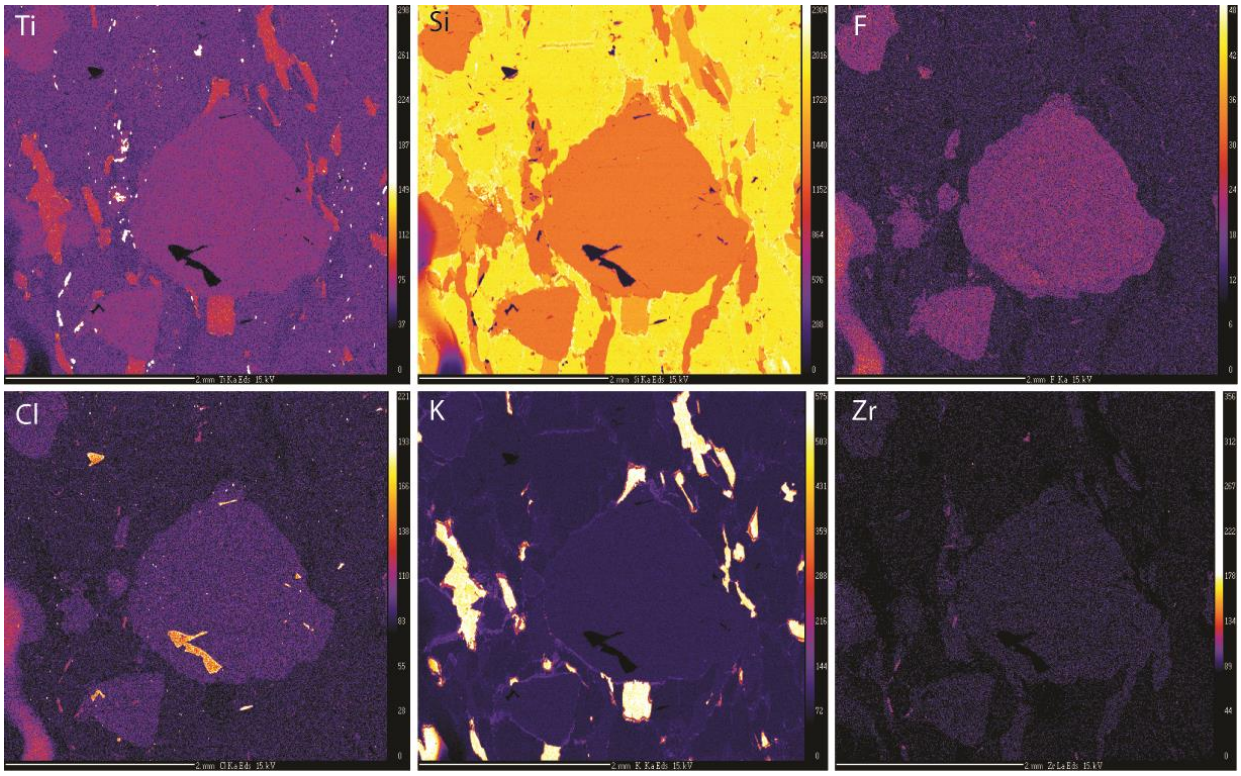

HOL7C_2014: SYMPLECTITES MAP

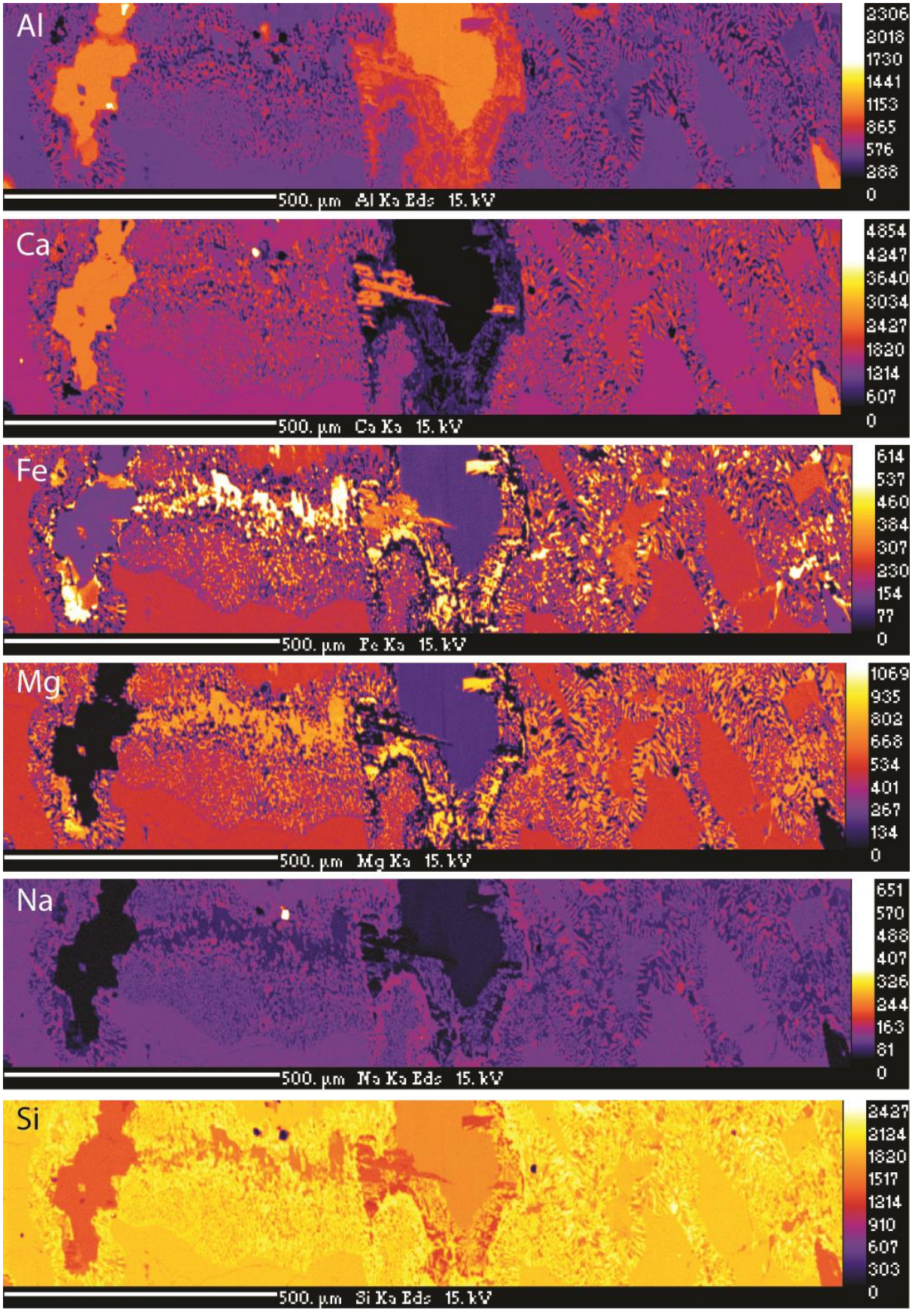

APPENDIX E: ADDITION MICROPROBE ANALYSIS DATA

HOL7C_2014

Symplectite: Light																							
SiO2	51.09	53.09	52.60	53.17	54.86	51.30	51.94	51.64	51.54	52.36	53.23	54.65	52.70	50.37	49.04	45.89	48.45	50.86	52.53	50.30	51.77	52.36	52.30	53.31
ZrO2	0.00	0.00	0.00	0.00	0.00	0.00	0.01	0.01	0.01	0.02	0.02	0.00	0.00	0.03	0.00	0.02	0.00	0.01	0.00	0.01	0.00	0.00	0.00	0.05
TiO2	0.20	0.22	0.24	0.17	0.16	0.19	0.23	0.24	0.25	0.20	0.20	0.15	0.21	0.27	0.28	0.52	0.30	0.23	0.17	0.27	0.26	0.17	0.21	0.17
ZnO	0.00	0.00	0.03	0.01	0.01	0.00	0.00	0.00	0.00	0.00	0.01	0.00	0.04	0.00	0.00	0.01	0.01	0.03	0.00	0.01	0.02	0.02	0.02	0.01
Al2O3	9.24	12.38	11.24	12.65	11.80	9.21	10.64	11.73	11.76	11.43	11.75	12.58	11.35	11.72	12.23	17.87	11.39	11.15	9.11	9.91	11.70	7.84	9.93	12.29
V2O3	0.06	0.02	0.04	0.01	0.05	0.08	0.06	0.04	0.07	0.03	0.05	0.03	0.05	0.07	0.04	0.06	0.05	0.03	0.04	0.05	0.05	0.04	0.07	0.03
Cr2O3	0.01	0.02	0.00	0.00	0.01	0.01	0.00	0.01	0.00	0.01	0.01	0.02	0.02	0.00	0.00	0.00	0.05	0.00	0.02	0.01	0.02	0.04	0.01	0.02
FeO	6.98	6.12	6.53	5.32	4.86	6.95	6.71	6.84	6.59	6.16	5.55	4.86	5.84	7.62	7.99	9.01	8.48	7.39	5.82	7.33	6.45	6.86	5.58	5.28
MnO	0.03	0.03	0.04	0.02	0.04	0.04	0.01	0.02	0.02	0.03	0.03	0.03	0.04	0.01	0.04	0.03	0.01	0.04	0.01	0.04	0.01	0.04	0.04	0.02
MgO	10.25	8.43	8.94	7.65	7.70	10.16	9.26	8.87	8.77	8.46	8.22	7.26	8.58	9.13	9.72	7.92	10.41	9.49	9.47	9.92	8.66	9.36	8.99	7.69
CaO	15.61	12.4	14.08	11.88	13.02	15.64	14.42	12.92	13.09	13.67	13.51	12.43	13.33	13.12	12.53	8.75	13.12	13.44	15.75	15.12	12.96	15.20	13.56	12.12
BaO	0.02	0.01	0.00	0.03	0.00	0.03	0.00	0.00	0.01	0.00	0.00	0.00	0.01	0.00	0.01	0.03	0.00	0.00	0.00	0.01	0.02	0.01	0.01	0.01
Na2O	4.44	5.55	5.10	6.36	6.21	4.43	4.86	5.27	5.14	5.70	5.71	6.38	5.55	5.05	4.48	5.08	4.52	4.93	4.98	4.64	5.13	4.74	4.65	5.78
K2O	0.26	0.32	0.29	0.49	0.15	0.23	0.26	0.37	0.38	0.21	0.18	0.16	0.22	0.47	0.63	1.31	0.57	0.40	0.11	0.24	0.36	0.38	0.57	0.38
P2O5	0.00	0.00	0.00	0.00	0.00	0.00	0.00	0.00	0.00	0.00	0.00	0.00	0.00	0.00	0.00	0.00	0.00	0.00	0.00	0.00	0.00	0.00	0.00	0.00
Cl	0.01	0.01	0.00	0.01	0.06	0.00	0.01	0.01	0.01	0.00	0.00	0.00	0.01	0.01	0.01	0.02	0.01	0.01	0.00	0.01	0.01	0.02	0.02	0.03
F	0.00	0.00	0.00	0.00	0.00	0.00	0.00	0.00	0.00	0.00	0.00	0.00	0.00	0.00	0.00	0.00	0.00	0.00	0.00	0.00	0.00	0.00	0.00	0.00
O	0.00	0.00	0.00	0.00	-0.01	0.00	0.00	0.00	0.00	0.00	0.00	0.00	0.00	0.00	0.00	0.00	0.00	0.00	0.00	0.00	0.00	0.00	0.00	-0.01
TOTAL	98.20	98.6	99.1	97.7	98.9	98.2	98.4	97.9	97.6	98.3	98.4	98.5	97.9	97.8	97.0	96.5	97.3	98.0	97.9	97.8	97.4	97.0	95.9	97.1

Symplectite: dark																		
SiO2	56.87	54.91	58.45	59.16	57.39	58.35	56.81	54.74	54.03	54.44	55.70	54.44	53.08	51.95	53.23	56.92	54.87	55.00
ZrO2	0.00	0.00	0.00	0.00	0.00	0.00	0.03	0.00	0.00	0.00	0.00	0.01	0.00	0.00	0.00	0.01	0.00	0.00
TiO2	0.17	0.22	0.25	0.15	0.10	0.08	0.09	0.21	0.13	0.14	0.13	0.23	0.28	0.08	0.24	0.13	0.13	0.14
ZnO	0.03	0.00	0.01	0.04	0.05	0.01	0.00	0.01	0.00	0.00	0.02	0.00	0.00	0.04	0.02	0.00	0.01	0.00
Al2O3	17.20	19.93	21.21	20.34	13.53	15.01	15.47	20.82	12.41	12.72	13.73	18.65	17.35	21.69	12.76	14.34	12.52	13.30
V2O3	0.02	0.03	0.02	0.00	0.04	0.00	0.03	0.05	0.06	0.04	0.06	0.03	0.04	0.03	0.06	0.05	0.07	0.05
Cr2O3	0.01	0.00	0.00	0.00	0.03	0.01	0.02	0.00	0.00	0.00	0.01	0.00	0.02	0.01	0.01	0.03	0.00	0.02
FeO	3.00	3.40	1.65	1.50	3.47	2.75	2.82	2.66	4.69	5.28	4.19	3.89	5.16	2.28	5.96	3.43	4.68	4.52
MnO	0.02	0.00	0.00	0.01	0.02	0.02	0.01	0.02	0.01	0.05	0.00	0.00	0.02	0.00	0.04	0.00	0.02	0.02
MgO	4.18	3.43	2.07	2.00	5.60	4.59	4.21	2.69	7.02	7.33	6.33	4.33	5.50	2.30	7.72	5.90	7.12	6.78
CaO	7.51	7.52	3.07	4.46	10.39	9.20	8.58	7.54	12.47	11.78	11.02	7.82	8.15	12.16	11.86	10.42	12.52	11.66
BaO	0.08	0.15	0.16	0.12	0.01	0.03	0.03	0.09	0.01	0.01	0.01	0.05	0.04	0.08	0.00	0.03	0.00	0.00
Na2O	7.63	7.17	9.03	8.97	7.40	7.84	7.61	7.45	5.87	6.19	6.93	7.07	7.16	5.81	5.85	7.19	6.39	6.57
K2O	0.55	0.87	1.20	0.63	0.10	0.09	0.25	0.76	0.18	0.25	0.24	0.73	0.62	0.29	0.35	0.12	0.14	0.18
P2O5	0.00	0.00	0.00	0.00	0.00	0.00	0.00	0.00	0.00	0.00	0.00	0.00	0.00	0.00	0.00	0.00	0.00	0.00
Cl	0.02	0.01	0.00	0.00	0.01	0.00	0.02	0.02	0.01	0.02	0.01	0.01	0.02	0.02	0.00	0.01	0.01	0.00
F	0.00	0.00	0.00	0.00	0.00	0.00	0.00	0.00	0.00	0.00	0.00	0.00	0.00	0.00	0.00	0.00	0.00	0.00
O	0.00	0.00	0.00	0.00	0.00	0.00	0.00	0.00	0.00	0.00	0.00	0.00	0.00	0.00	0.00	0.00	0.00	0.00
TOTAL	97.30	97.66	97.12	97.39	98.13	97.98	95.98	97.06	96.90	98.22	98.38	97.26	97.41	96.74	98.10	98.57	98.47	98.25